Check for updates

Decoupling electrode kinetics to elucidate reaction mechanisms in alkaline water electrolysis

Woo Yeong Noh,[a] Samuel J. Kazmouz, [b] Seong-hun Lee,[c] Jui-Kun Peng,[b] Tae Joo Shin[c] and Meital Shviro [*a]

Alkaline water electrolysis (AWE) presents key advantages, including reduced material costs, enhanced operational stability, and compatibility with non-precious metal catalysts, positioning it as a scalable route for hydrogen production. In this study, we introduce a minimally invasive single-cell configuration incorporating a reference electrode *via* diaphragm extension to form an internal ion channel. This setup, combined with an interfaced potentiostat and auxiliary electrometer, enables real-time, independent monitoring of anode and cathode behavior, offering high-resolution electrochemical diagnostics. While it is well established that the hydrogen evolution reaction (HER) exhibits sluggish kinetics in alkaline media, our study reveals that this limitation persists even in practical AWE systems where nickel-based substrates are used as electrodes. This observation is supported by both experimental data and voltage breakdown modeling. Arrhenius-type analysis reveals that localized electric fields induced by catalysts shift the reaction kinetics from classical Butler–Volmer behavior toward a Marcus-like regime, where interfacial molecular dynamics and bimolecular charge transfer dominate. We propose a semi-empirical model and a surficial reaction mechanism to describe these dynamics. This work underscores the critical need for cathode innovation and provides a rational framework for designing advanced catalysts and electrode architectures to optimize AWE performance.

Broader context
Alkaline water electrolysis (AWE) offers a cost-effective pathway, especially with non-precious metal catalysts, but progress is hindered by a limited understanding of electrode-specific performance under real-conditions. This study introduces a reference electrode-integrated electrolysis platform to uncover kinetic bottlenecks in hydrogen production, revealing that the hydrogen evolution reaction is more sluggish than conventionally assumed. By establishing a new kinetic model and mechanistic insights, this work offers practical strategies to improve AWE design and efficiency, contributing to the deployment of robust and low-cost electrolyzers.

Introduction

Among electrolysis technologies, alkaline water electrolysis (AWE) stands out as one of the most mature and viable options for large-scale hydrogen generation, owing to its use of cost-effective and earth-abundant catalyst materials and cell components.[1,2] However, AWE suffers from relatively low efficiency, particularly at low current densities, where high overpotentials are primarily attributed to large overpotentials

associated with the hydrogen evolution reaction (HER) and oxygen evolution reaction (OER).[3,4] In AWE systems, nickel-based materials are widely used as support materials and often as catalysts, valued for their stability in concentrated alkaline environments. Yet, a clear understanding of the kinetics of HER and OER at the individual electrode level remains lacking, despite its importance for rational electrode and catalyst design.

To evaluate the performance of individual electrodes, a reference electrode (RE) is needed between the anode and cathode. However, placing an RE in a zero-gap cell is challenging, as it can alter the cell geometry and potentially affect system behavior. Various approaches have been explored to integrate dynamic hydrogen electrodes (DHE) or quasi-reference electrodes (such as Pt wires) in polymer electrolyte membrane (PEM) fuel and electrolysis cells.[5] Quasi-REs often

[a] *National Renewable Energy Laboratory (NREL), Golden, Colorado 80401, USA.*
E-mail: meital.shviro@nrel.gov
[b] *Argonne National Laboratory (ANL), Lemont IL 60439, USA*
[c] *Graduate School of Semiconductor Materials and Devices Engineering,*
Ulsan National Institute of Science and Devices Engineering,
Ulsan National Institute of Science and Technology (UNIST), Ulsan 44919,
Republic of Korea

This journal is © The Royal Society of Chemistry 2025

Energy Environ. Sci., 2025, **18**, 8679–8696 | 8679

exhibit unstable potentials, influenced by their local environment, while DHE electrodes suffer from poor stability in highly concentrated alkaline electrolytes.[6] Additionally, integrating an RE within a zero-gap configuration poses practical difficulties, such as the risk of bubble formation, which can disrupt ionic contact, and the introduction of additional ionic resistance that may distort potential measurements.[7] Furthermore, improper placement or misalignment of the RE can affect the local electrochemical environment, leading to inaccuracies in diagnosing HER and OER kinetics.[8] More recently, Leuaa *et al.* introduced a refined method for integrating a reference electrode into a zero-gap AWE cell.[9] The approach involved extending a section of the Zirfon diaphragm and modifying the gasket to enable the extended strip to protrude from the cell into an external electrolyte bath of identical concentration, ensuring stable and accurate potential measurements.

In this study, we adopt an extended-strip-based reference electrode integration approach and uniquely implement a dual-instrumentation configuration—combining an interfaced potentiostat with an auxiliary electrometer—to enable simultaneous, independent monitoring of anode and cathode behavior during operation. Using nickel foam as the baseline electrode material, this setup provides high-resolution insight into individual electrode performance under realistic AWE conditions. Notably, we reveal that HER, despite its mechanistic simplicity, emerges as the kinetic bottleneck in AWE when catalyst is not integrated. Cell modeling was employed to validate consistency with experimental results, and the computed electrochemical parameters were used to perform a voltage breakdown, enabling the identification of kinetic, ohmic, and mass transport behaviors at both the cathode and anode. X-ray absorption fine structure (XAFS) analysis, in conjunction with our dual-instrumentation electrochemical measurements, revealed key material-activity relationships, including degradation mechanisms of nickel foam and structural evolution within the catalyst layer following catalyst introduction. Crucially, Arrhenius-type analysis showed a mechanistic shift in the presence of a catalyst: while activation energy decreases with overpotential increase under catalyst-free conditions (consistent with the classical Butler–Volmer model),[10,11] it becomes overpotential-independent when a catalyst is introduced. Instead, the pre-exponential factor (A) rises exponentially with overpotential increase, indicating a transition to Marcus-type behavior where interfacial molecular dynamics and bimolecular charge transfer dominate. This shift led us to propose a new surficial molecular reaction mechanism: localized electric fields and dipole modulation within the catalyst layer promote water structuring, dynamic protonation/deprotonation, and enhanced intermolecular charge transfer at the electrode–electrolyte interface.

Results and discussion

Validation of the experimental setup

Fig. 1a illustrates the configuration of the reference electrode (RE)-integrated zero-gap alkaline cell and the interfacing of measurement equipment used to record cell voltage and the individual electrode potential simultaneously. To establish an ion channel between the alkaline cell and the RE (a customized Hg/HgO electrode filled with 30% KOH solution, calibrated for RHE conversion using RDE techniques) (Fig. S1, SI), we utilized an open-type Zirfon diaphragm gasket in combination with an external electrolyte bath (Fig. S2, SI).[8,12] This configuration, illustrated in Video S1, enables continuous electrolyte flow through an extended diaphragm strip, maintaining hydration and ensuring consistent ion conduction throughout operation. The experimental setup incorporates a potentiostat equipped with a booster, which facilitates the application and measurement of cell voltage or current. Additionally, an auxiliary electrometer is employed to independently measure the potential and current of both the anode and the cathode. To validate the setup, polarization curves and electrochemical impedance spectroscopy (EIS) data for the full cell were compared with individual electrode measurements, showing a strong correlation (Fig. S3a–c, SI). High frequency resistance (HFR) corrections applied using EIS data above 1 kHz (Fig. S3d, SI), compensated for interfacial and solution resistances, including those from the reference electrode. Reproducibility tests showed minimal deviations at low currents, while variations up to 50 mV (Fig. S4, SI) at high currents were attributed to bubble management issues, which were mitigated by HFR corrections. Thus, all analyses in this study used HFR-corrected data. To further evaluate the robustness of the dual-instrumentation setup, additional experiments were performed using a thinner 220 μm diaphragm and nickel mesh as electrode materials. Employing the thinner diaphragm reduced ohmic resistance for both the cathode and anode, improving ion transport efficiency and leading to enhanced performance, particularly in the intermediate current density range where ion transport limitations start to become significant (Fig. S5, SI). When nickel mesh was used, performance differences were observed mostly for the anode, resulting in lower cell performance compared to the foam, this aligns with expectations, as the reduced surface area of the mesh limit reaction sites, impacting electrochemical activity (Fig. S6, SI). These findings underscore the versatility and reliability of the dual-instrumentation setup in accurately assessing cell performance across diverse configurations and materials.

HER *vs.* OER: which one is a key player?

Electrochemical analysis comparing cathode and anode behavior reveals consistently greater overpotential for the cathode (HER) than for the anode (OER) across all current densities (Fig. 1b). Notably, the cathode exhibits higher HFR, which is not fully explained in the literature, but may be influenced by variations in OH$^-$ concentration, increased contact resistance at the electrode–electrolyte interface, and local ion depletion caused by hydrogen nanobubble formation. Optimal ionic conductivity occurs at 30 wt% KOH, and deviations from this concentration can reduce ion mobility. While further investigation is needed to elucidate the precise mechanisms, reproducibility tests have consistently confirmed these observations. Fig. 1c–f present Nyquist plots and distribution of relaxation times (DRT)
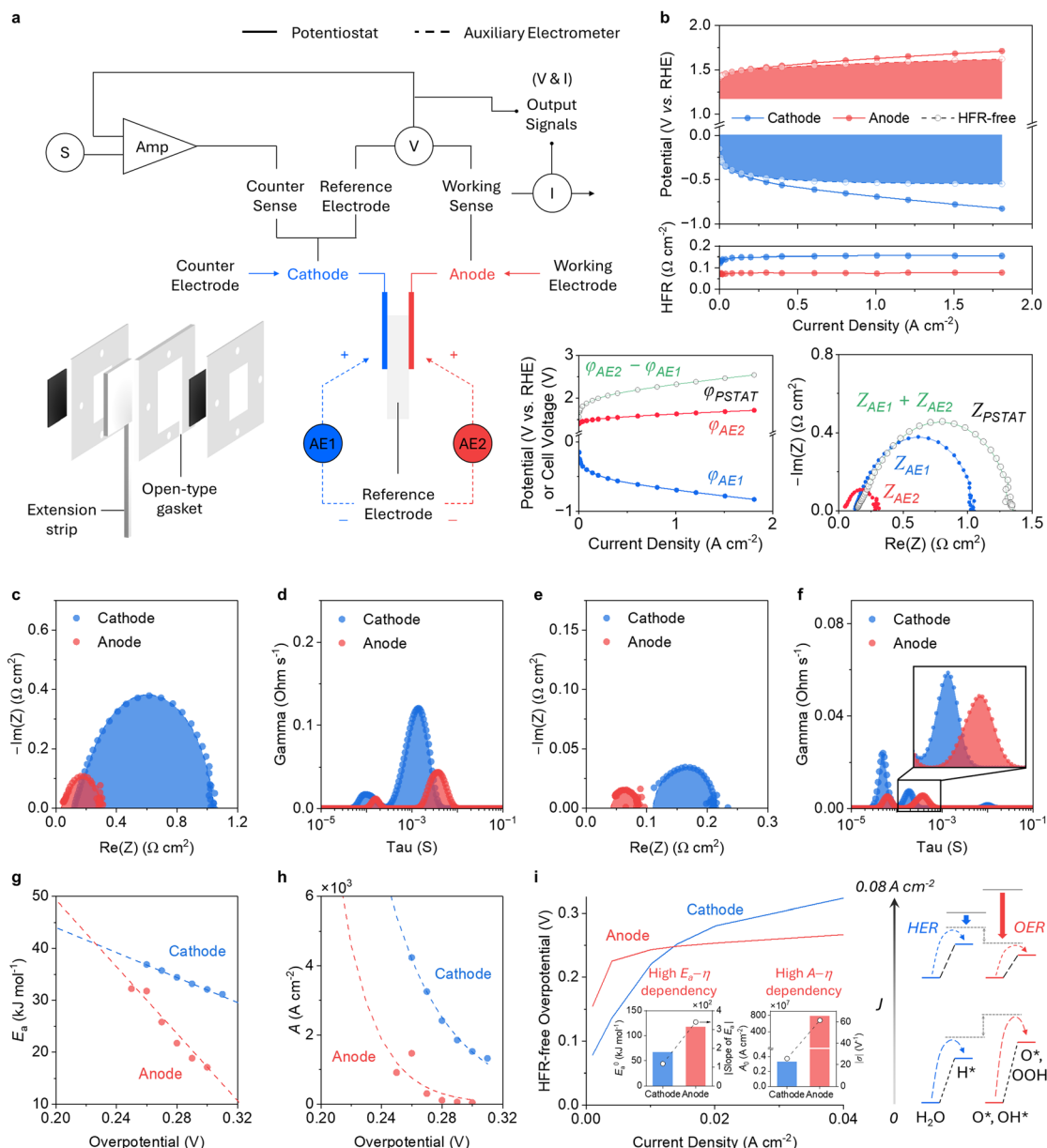
8680 | *Energy Environ. Sci.*, 2025, **18**, 8679–8696

This journal is © The Royal Society of Chemistry 2025

Fig. 1 Integration of a reference electrode in a dual instrumentation setup for alkaline water electrolysis and electrochemical comparison of the cathode and anode with a nickel foam substrate. (a) Schematic illustrating the sensing lead configuration of the interfaced potentiostat and auxiliary electrometer, enabling voltage, potential, and impedance measurements in galvanostatic mode. (b) Polarization curves with HFR, where the shaded regions indicate overpotential calculated from the equilibrium potential derived *via* cell modeling. (c)–(f) Nyquist plots and DRT spectra at 0.08 A cm^{-2} (c) and (d) and 1.0 A cm^{-2} (e) and (f). (g) and (h) Arrhenius-type analysis to elucidate the dependence of apparent activation energy (E_a) and pre-exponential factor (A) on overpotential. Note that E_a decreases linearly (eqn (2)), while A decreases exponentially (eqn (3)). (i) Left, correlation between electrochemical activity at low current densities and kinetic descriptors. The HFR-free overpotential plot includes inlets showing equilibrium-state E_a and its slope, as well as A and its coefficient (σ) fitted using the semi-empirical equation. Right, Illustrative depictions of energy barrier variations for HER and OER as current density increases in the low-current region.

spectra for both electrodes at low (0.08 A cm^{-2}) and high (1.0 A cm^{-2}) current densities. A significantly larger semicircle in the cathode's Nyquist plot indicates higher charge transfer resistance (0.95 *vs.* 0.27 Ω cm^{-2}) (Fig. 1c and Fig. S7, SI), consistent with the dominant DRT's peak in the kinetic frequency region (Fig. 1d and Fig. S8, SI) and a steeper Tafel slope (143 *vs.* 51 mV dec^{-1}, Fig. S9, SI). These findings suggest that HER shows higher charge transfer resistance and slower kinetics

than OER, as evidenced by the cathode's Nyquist and DRT analyses (Fig. 1e and f).[13]

The consistently higher ohmic resistance observed at the cathode may be partially attributed to mass or ion transport limitations, possibly exacerbated by local nanobubble trapping within the pores near or between the diaphragm and electrode.[14] This is hypothesized to be affected by the stronger adhesion of the hydrogen bubbles to the porous nickel foam

This journal is © The Royal Society of Chemistry 2025

Energy Environ. Sci., 2025, **18**, 8679–8696 | **8681**

due to higher surface tension, causing a "pinning effect" that hinders their removal and obstructs reactant access.[15–18] The increased resistance, particularly in zero-gap cells, where micro-gaps between the electrode and diaphragm exacerbate mass transport limitations and amplify the ohmic drop compared to oxygen bubbles. Although Ni foam is not a deliberately engineered catalyst, it can develop surface phases such as $Ni(OH)_2$ or $NiOOH$ under alkaline operating conditions, which offer moderate OER activity. In contrast, its intrinsic HER activity remains limited, leading to significantly higher overpotentials on the cathode side. These asymmetric electrode behaviors, clearly captured by the dual-instrumentation tool, highlight HER as the dominant kinetic bottleneck under catalyst-free conditions and underscore the necessity of introducing HER-active materials to enhance full-cell performance.

To further investigate HER and OER kinetics during AWE, Arrhenius-type analysis was further conducted using the equation:

$$J = A e^{-\frac{E_a}{RT}} \qquad (1)$$

where A is the pre-exponential factor, E_a is the apparent activation energy, R is the ideal gas constant, T is the temperature, and J is the current density. Cathode and anode potentials were analyzed at current densities below 0.5 A cm^{-2} (where mass transport effects are negligible) across temperatures of 40 °C, 60 °C, and 80 °C (Fig. S10, SI). Since all experiments were conducted in the same concentration of KOH, allowing direct comparisons without normalization to the unit concentration of the reactant, A retains the same unit as J (A cm^{-2}).[19,20] For overpotential calculations, equilibrium potentials were obtained through a modeling study that incorporated the reversible potential and concentration correction-adjusted Nernst potential at each temperature. For the full and half-cells, the reversible potential included a temperature correction. Subsequently, the Nernst potential was calculated using the corrected reversible potential and an activity (or concentration) correction with special consideration to the activities of OH^- and H_2O, due to the high concentration of electrolyte. More details on the calculation of the Nernst potential are discussed in subsequent sections. Using cubic spline fitting and interpolation, currents at fixed overpotentials were extracted, and Arrhenius plots were constructed to determine slopes and y-intercepts indicating E_a and A, respectively (Fig. 1g and h). Under the assumption that the system follows the classical Butler–Volmer model,[10,11] we can combine the two equations as follows to define the relationship between activation energy and overpotential:

$$E_a = E_a^0 - \alpha n F \eta \qquad (2)$$

where E_a is the apparent activation energy, E_a^0 is the equilibrium activation energy, α is the charge transfer coefficient, n is the number of electrons transferred, F is the Faraday constant, and η is the overpotential. The apparent E_a for HER decreases linearly from 36.9 kJ mol^{-1} at 0.26 V to 31.1 kJ mol^{-1} at 0.3 V. In comparison, for OER, the apparent E_a shows a more pronounced decline from 32.2 kJ mol^{-1} to 17 kJ mol^{-1} over a similar overpotential range. This enhanced sensitivity in OER is likely due to its greater number of electron transfer steps resulting in a higher effective α-value compared to HER. As a result, the kinetics of OER accelerate more rapidly with increasing η, which explains why the relative efficiency of HER becomes increasingly limited at higher overpotentials.

An empirical exponential relationship between A and η was observed, as described by:

$$A = A_0 e^{\sigma \eta} \qquad (3)$$

Here, A_0 is the equilibrium pre-exponential factor and σ is defined as surface reactivity, serving as a dynamic indicator of the reaction rate on the electrode surface. However, rather than being a simple quantitative indicator, it is reinterpreted as a relative surface dynamic contribution factor, reflecting the extent to which the probability of reaction occurrence and the facilitation of reaction progression at the electrode–electrolyte interface influence overall reaction kinetics under potential-induced changes. Generally, σ is a physical quantity that assumes positive values; however, under certain non-equilibrium conditions, particularly when ion adsorption and desorption at the electrode–electrolyte interface become asymmetric, σ may take on negative values due to dynamic charge redistribution or changes in active site availability.[21] In this context, nickel foam may struggle to optimize its interfacial structure for electron transfer as overpotential increases, while inefficient bubble removal further lowering A. When activation energy dominates reaction rates, surface reactivity plays a minor role. Additionally, real electrochemical reactions follow multiple pathways, deviating from the Butler–Volmer model, which can lead to non-constant or even negative σ values under certain conditions.

The lower A_0 observed for HER compared to OER suggests that a less efficient interfacial structure is initially formed at the cathode. In contrast, the weaker inverse dependence of A on η at the cathode implies that the interfacial structure can reorganize more dynamically in response to overpotential variations, likely due to the intrinsic simplicity of the HER pathway, which enables more efficient molecular reorganization at higher overpotentials.[22] Nevertheless, due to the greater kinetic constraint associated with the Volmer step[23] for HER on nickel foam compared to the formation of O, OH, and OOH intermediates in OER, the reaction rate at the cathode remains predominantly governed by the activation energy rather than the pre-exponential factor. Consequently, the activation energy, along with the charge transfer efficiency (α), becomes the dominant kinetic descriptor, as reflected in the weaker η-dependence of the E_a observed at the cathode. This mechanistic distinction explains why HER initially exhibits a lower overpotential than OER at ultra-low current densities (e.g., 0.004 A cm^{-2}) but is surpassed by OER at slightly higher current densities, such as 0.014 A cm^{-2} (Fig. 1i). While HER benefits from a lower intrinsic energy barrier at equilibrium, the higher α-value for OER enables a more effective reduction in activation energy with increasing overpotential, leading to superior activity at elevated current densities. Therefore, when nickel foam is used as both electrodes, the overall lower HER efficiency stems from its limited ability to dynamically lower E_a compared to OER under practical AWE conditions.

8682 | Energy Environ. Sci., 2025, **18**, 8679–8696

This journal is © The Royal Society of Chemistry 2025

Catalyst's kinetic behaviors on the nickel foam

Fig. 2a and b present the polarization curves and Nyquist plots for the system with Pt/C as the cathode catalyst and NiFe as the anode catalyst (Pt/C + NiFe (both)), with a reference case using nickel foam as both cathode and anode without integrated catalysts included for comparison. Additional control cases, where a catalyst is introduced at either the cathode or the anode alone (Pt/C (cathode) or NiFe (anode)), were investigated. Catalyst introduction resulted in a clear potential gain at both electrodes, with a particularly pronounced effect at the cathode,
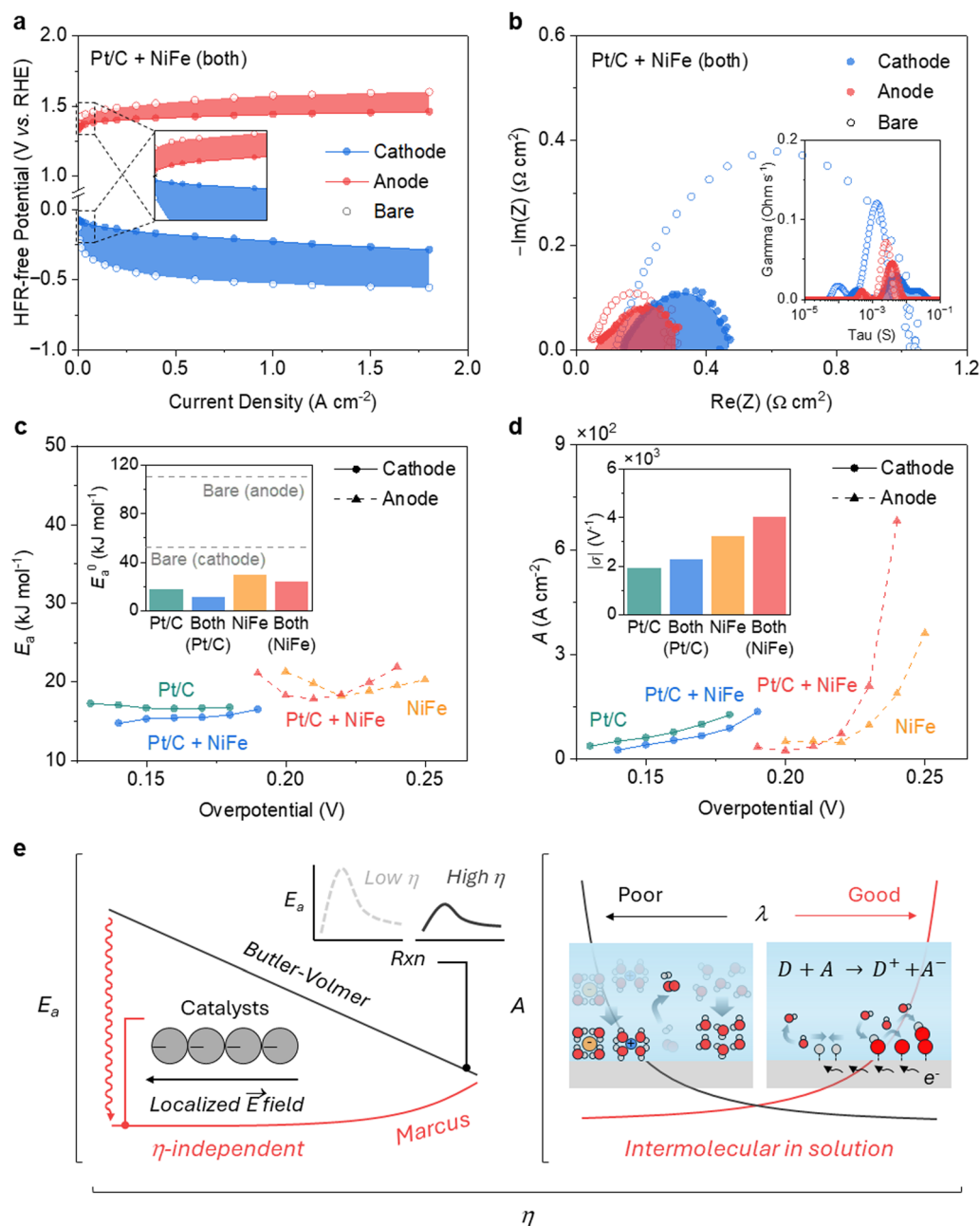

Fig. 2 Kinetic analysis of catalyst introduction at the cathode and anode. (a) HFR-free polarization curves, where shaded regions indicate potential gain relative to the nickel foam reference case without integrated catalysts. A Pt/C catalyst (0.5 mg cm^{-2}) was applied at the cathode, while a NiFe catalyst (1.0 mg cm^{-2}) was used at the anode, collectively denoted as Pt/C + NiFe (both). (b) Nyquist plots at 0.08 A cm^{-2}, with solid dots and shaded regions representing cases with catalysts, while hollow dots indicate cases without integrated catalysts. The inset in (b) corresponds to the associated DRT spectra. (c) E_a as a function of overpotential. The inset in (c) corresponds to the associated equilibrium E_a. (d) A as a function of overpotential. The inset in (d) represents the coefficient (σ) fitted using the semi-empirical equation. Plots (c) and (d) also include additional catalyst configurations: Pt/C at the cathode with bare nickel foam at the anode (Pt/C (cathode)) and NiFe alloy at the anode with bare nickel foam at the cathode (NiFe (anode)). (e) Illustrative depiction of possible reaction models with and without integrated catalysts. Note: with catalyst introduction, E_a remains constant (eqn (2)), while A instead increases exponentially (eqn (3)). Due to the electric dipole formed within the catalyst layer under an external electric field, the catalyst-induced reduction in the energy barrier remains constant with increasing overpotential. Instead, charge transfer at the catalyst surface becomes the dominant factor governing the reaction rate.

significantly contributing to overall full-cell performance improvement (Fig. 2a and Fig. S11, SI). This was further verified by impedance analysis, where EIS and DRT results at low current densities (0.08 A cm^{-2}) revealed a substantial charge transfer gain, particularly at the cathode (Fig. 2b and Fig. S12, SI). Additionally, the enhancement of the electron transfer coefficient (α) and the reduction of kinetic losses at each electrode, especially at the cathode, further reinforced these findings (Fig. S13, SI). Notably, in the Pt/C (cathode) and NiFe (anode) combinations, the electrode with the catalyst exhibited a clear kinetic gain, whereas the opposing electrode (bare nickel foam) displayed potential and impedance characteristics similar to the reference case. These findings support the fact that the insufficient HER activity of nickel foam remains a major bottleneck in AWE cell performance. Furthermore, to evaluate the diagnostic sensitivity of the dual-instrumentation tool, control experiments were conducted using catalysts with poor activity for either HER or OER—namely, NiO and Co_3O_4 at the cathode and Pt/C at the anode. When NiO or Co_3O_4 were used at the cathode, improvements in HER activity and charge transfer efficiency were minimal (Fig. S14, SI). In contrast, using Pt/C at the anode led to a decline in OER performance and charge transfer efficiency (Fig. S15, SI). Separately, at high current densities, impedance similar to that of bare nickel foam was observed regardless of the catalyst configuration (Fig. S16, SI), suggesting that the benefits of catalysts for mass transport are limited under these conditions. As the loading of Pt/C and NiFe catalysts increased, charge transfer resistance remained unchanged, while noticeable activity enhancements in the low current density region were observed (Fig. S17 and S18, SI), indicating that factors beyond simply reducing energy barriers and adding active sites significantly contribute to kinetic enhancement. This study suggests that these additional contributions arise from interfacial molecular dynamics, which are likely enhanced as catalyst loading increases. Such effects include the orientation or reorganization of adsorbates and surrounding water molecules, hydroxide adsorption/desorption, and surface restructuring on the catalyst, which may play a dominant role in governing reaction kinetics.[24]

To gain deeper insights into HER and OER kinetics, Arrhenius-type analysis was further conducted following the outlined methodology (Fig. S19–S21, SI). Unlike "without integrated catalysts" systems, where E_a linearly decreases with increasing overpotential, we observed a completely distinct behavior upon catalyst introduction: E_a remained nearly independent of overpotential, while A exhibited an exponential increase (Fig. 2c and d). First, through a comparison of equilibrium activation energy, it was evident that the catalyst effectively lowered the energy barrier, reducing E_a^0 for HER and OER by approximately 3.8-fold and 4-fold, respectively, compared to the reference case. For HER, E_a was 17 ± 0.4 kJ mol^{-1} for Pt/C (cathode) and 15.6 ± 0.9 kJ mol^{-1} for Pt/C + NiFe (both). Similarly, for OER, E_a was 20.4 ± 2.3 kJ mol^{-1} for NiFe (anode) and 20 ± 2.2 kJ mol^{-1} for Pt/C + NiFe (both). This deviation from the Butler–Volmer model, where the reaction rate increases as overpotential rises due to a reduction in the energy

barrier for charge transfer, suggests that E_a is no longer the dominant factor in determining the reaction rate (α is nearly negligible according to eqn (2)).

Instead, the reaction rate is mainly governed by interfacial molecular dynamics, as shown by the exponential rise of both the pre-exponential factor (A) and the surface reactivity parameter (σ) with increasing overpotential. Fig. 2e illustrates a proposed reaction model based on E_a–η and A–η relationships, highlighting the role of interfacial molecular dynamics. It is hypothesized that catalyst layers modulate localized electric fields, enhancing interfacial reorganization energy, stabilizing reaction intermediates, and enabling multi-step charge transfer processes. According to Marcus's theory, excessive spontaneity in free energy at high overpotentials leads to the emergence of an "inverted region", where activation energy rises again.[25] Consistent with this, the Arrhenius-type analysis results for particle-type catalyst-integrated cases suggest that electrodes in AWE behave more like the Marcus model, entering an inverted region where activation energy starts increasing again at high overpotential. Under these conditions, the reaction kinetics are primarily determined by intermolecular electron transfer processes governed by interfacial molecular dynamics.

These factors collectively lead to a different A–η relationship and a distinct range of values upon catalyst introduction under favorable energetic conditions ($\eta > 0$). Notably, the previously established semi-empirical A–η equation exhibited excellent agreement with experimental data fitting results, achieving an R^2 value exceeding 0.98 (Fig. S22, SI). The observation that the A_0 of the Pt/C cathode catalyst is larger than that of the NiFe anode catalyst suggests that, along with a lower energy barrier, improved interfacial dynamics enable comparable or even more efficient intermediate H_{ads} formation in HER compared to the formation of OER intermediates. However, OER still exhibited a stronger overpotential dependence of A, represented by a larger σ, indicating that the adaptability of A to overpotential variations is primarily governed by the inherent complexity and multi-step nature of the reaction pathways.

Despite catalytic improvements, with potential gains of 50–55 mV for HER and 60–67 mV for OER at low current densities upon catalyst introduction, OER still exhibits a higher overpotential at ultra-low currents (0.004 A cm^{-2}) due to its inherently complex multi-step nature, as evidenced by its higher E_a^0 and η. This highlights the greater challenge of optimizing OER kinetics compared to HER, even with catalysts. Analysis of E_a and A across catalyst configurations (Fig. S23) revealed that when a catalyst was applied to only one electrode, the rate-determining step (RDS) at the opposite electrode influenced the overall cell E_a, making it η-dependent. However, introducing catalysts at both electrodes removed this dependency, stabilizing E_a that remained independent of η while causing A to increase exponentially. This highlights the crucial role of catalyst synergy and balanced surface dynamics in enhancing reaction efficiency.

Cell modeling for voltage breakdown

To strengthen the analysis and gain insight into the zero-gap alkaline cell setup a voltage breakdown model is developed.

8684 | *Energy Environ. Sci.*, 2025, **18**, 8679–8696

This journal is © The Royal Society of Chemistry 2025

The cell, anode, and cathode potentials are divided into the Nernst potential and kinetic (or activation), ohmic, and mass transfer overpotentials. The cell Nernst potential depends on the reversible potential and a concentration correction:[26,27]

$$E_{\text{Nernst}} = E_0 + \frac{RT}{2F} \log\left(\frac{\left(p_{H_2}^c\right)\left(p_{O_2}^a\right)^{0.5}}{p_0^{3/2} a_{H_2O}} \right) \qquad (4)$$

where E_a is the reversible potential, R is the universal gas constant, T is the temperature, F is Faraday's constant, $p_{H_2}^c$ and $p_{O_2}^a$ are the partial pressures of hydrogen at the cathode and oxygen at the anode, respectively, p_0 is the reference pressure, and a_{H_2O} is the activity of water. The Nernst potentials for the anode and cathode, independently, are calculated in a similar fashion with special consideration to the activity coefficient of OH$^-$, because concentration cannot be used as a proxy for activity in the Nernst equation due to non-ideal behavior at high ionic strengths.[28]

The ohmic overpotential across electrodes is modeled using a distributed current model which relies on the sheet resistance and Tafel slope.[29] In addition, the electrode ohmic overpotential accounts for the catalyst layer thickness which is estimated from the catalyst density, porosity, and mass to be around 2–3 μm. The ohmic overpotential across the diaphragm (η_{ohm}^s) is then defined as:

$$\eta_{\text{ohm}}^s = i \frac{d^s}{\sigma_{\text{KOH}} \times \frac{\phi^s}{\tau^s}} \qquad (5)$$

where d^s, ϕ^s, τ^s are the diaphragm thickness, porosity, and tortuosity, respectively, and σ_{KOH} is the electrolyte conductivity. The diaphragm resistance was estimated to be $\sim$135 mΩ cm^2,[30] aligning with HFR values extracted from EIS: $\sim$140 mΩ cm^2 for the bare configuration and $\sim$185 mΩ cm^2 for the Pt/C + NiFe case. This deviation is likely attributed to a combination of factors, including variations induced by the use of porous electrodes, compression during cell assembly, and intrinsic uncertainties associated with EIS measurements.[31] The asymmetric diaphragm resistance split observed between the cathodic and anodic sides can be attributed to localized hydrogen nanobubble accumulation at the cathode–diaphragm interface.[15,16] Given hydrogen's smaller bubble size and stronger surface adhesion compared to oxygen, a higher degree of nanobubble trapping is expected not only within the porous nickel foam but also within the skin layer of the Zirfon diaphragm on the cathode side.[14] This accumulation locally impedes ion transport, thereby increasing both through-plane and in-plane resistances more significantly at the cathode interface compared to the anode. To correct for these effects, the sheet resistance was partitioned based on a transmission line model (TLM) analysis, which exhibited strong agreement with experimental EIS measurements, resulting in an 60–75% of the total diaphragm resistance to the cathodic half-cell and 25–40% to the anodic half-cell, depending on the experimental configuration (Fig. S24, S25 and Table S1, SI). However, further experimental and modeling efforts are needed to verify this effect and assess its generality across different cell architectures.

The kinetic or activation overpotential is modeled after Butler–Volmer kinetics using a Tafel slope and an inverse hyperbolic sine function:

$$\eta_{\text{kin}} = b \times \sinh^{-1}\left(\frac{i}{i_0(1-\phi)} \right) \qquad (6)$$

where b is the Tafel slope, i_0 is the exchange current density, and φ is the surface bubble coverage or inactive area due to bubble coverage.[27] In addition, any deviation from the linear Tafel behavior is attributed to mass transfer limitations and modeled as:

$$\eta_{\text{mt}} = b_{\text{mt}} \times \ln\left(1 - \frac{i}{i_{\text{lim}}} \right) \qquad (7)$$

where b_{mt} is the mass transfer slope and i_{lim} is the limiting current density.[32,33] The parameters used in the modeling are summarized in Table S2 (SI). Using this approach, experimental polarization curves and overpotentials were used to validate the model output for each electrode and the full cell at 1 atm and 80 °C.

Polarization fitting across the full current density range was first performed for all catalyst configurations, including bare Ni foam reference, at 40 °C, 60 °C, and 80 °C, showing strong alignment with experimental data, thereby enabling reliable voltage breakdown analysis. (Fig. 3a, b, and Fig. S26–S28, SI). Kinetic loss modeling revealed that, for bare nickel foam, the HER overpotential exceeded the OER overpotential from as low as 0.12 A cm^{-2}, resulting in significant voltage loss in the low-current-density regime (Fig. 3c). Catalyst introduction substantially mitigated these losses (Fig. 3d). As summarized in Table S3 (SI), in the Pt/C + NiFe (both) configuration, the overall HER Tafel slope decreased from 144–166 mV dec^{-1} (bare Ni foam) to 43–48 mV dec^{-1}, and the HER kinetic overpotential was reduced from 305.5 mV to 73.5 mV at 0.08 A cm^{-2}, achieving a 75.9% improvement. In the Pt/C (cathode) control case—where Pt/C was introduced only at the cathode—the HER Tafel slope reached 39.6 mV dec^{-1} and the HER kinetic overpotential was 78 mV, closely matching the values observed in the Pt/C + NiFe (both) system. This confirms that the improved HER kinetics primarily originate from the Pt/C catalyst at the cathode. Similarly, for OER, in the Pt/C + NiFe (both) case, the OER Tafel slope was reduced from 58–62 mV dec^{-1} (bare Ni foam) to 42–43 mV dec^{-1}, and the OER kinetic overpotential decreased from 322.7 mV to 243.3 mV at 2 A cm^{-2}, corresponding to a 24.6% reduction. In the NiFe (anode) control case—where NiFe was applied only at the anode—the OER Tafel slope was measured as 47.5 mV dec^{-1}, and the OER kinetic overpotential as 253 mV, again comparable to the Pt/C + NiFe (both) configuration. Furthermore, TLM analysis of kinetic resistance confirmed that the Pt/C cathode catalyst led to a much more substantial reduction in charge transfer resistance compared to the NiFe anode catalyst (Fig. S30 and Table S4, SI). All these results collectively demonstrate that the voltage breakdown modeling reliably captures the experimentally observed trends, and that the kinetic improvements for HER and OER are
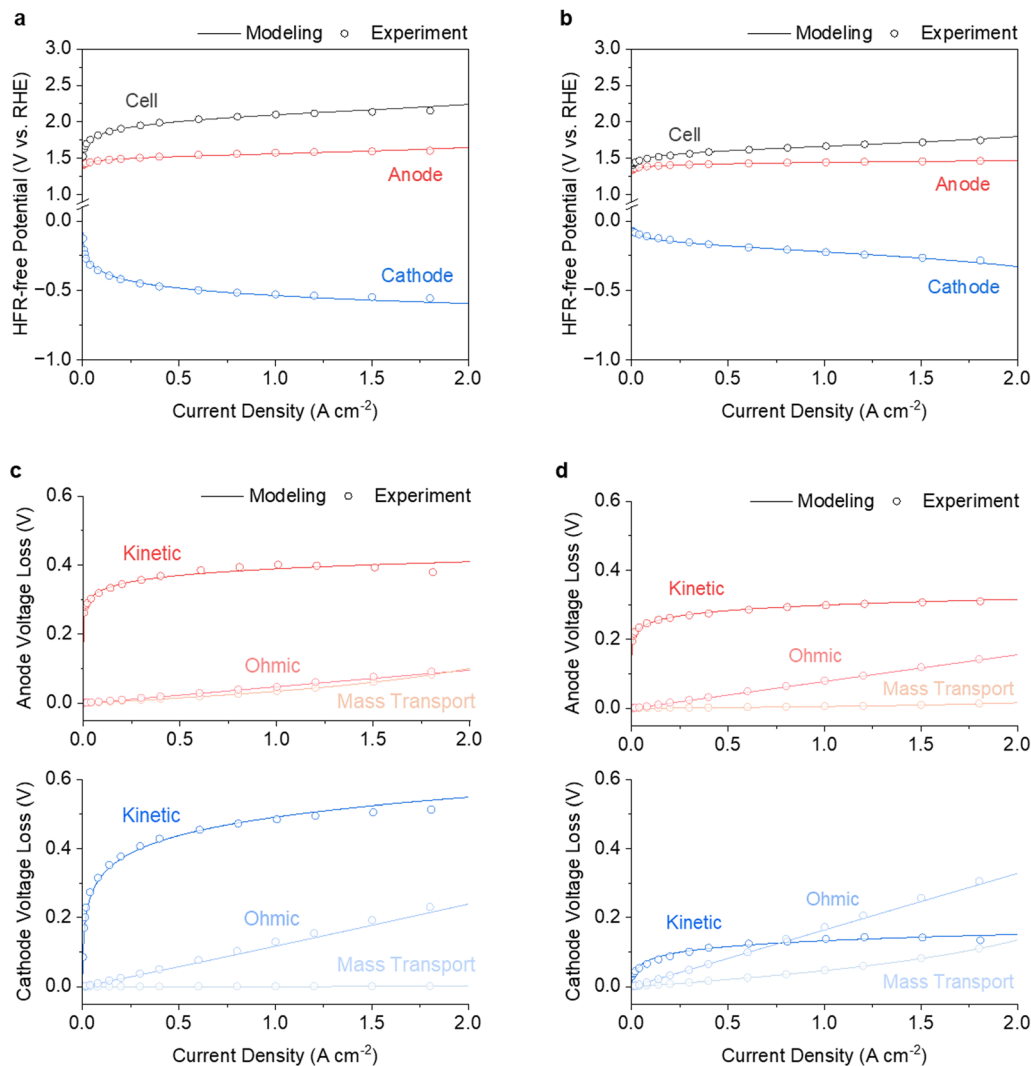
This journal is © The Royal Society of Chemistry 2025

Energy Environ. Sci., 2025, **18**, 8679–8696 | **8685**

Fig. 3 Modeling analysis for each electrode and full cell at 1 atm and 80 °C. (a) and (b) Comparison of experimental (hollow circles) and modeled (solid lines) HFR-free polarization curves for the bare nickel foam reference (a) and Pt/C + NiFe (both) configuration (b). (c) and (d) Voltage breakdown results for the bare nickel foam reference (c) and Pt/C + NiFe (both) configuration (d), with anodic and cathodic contributions shown in the upper and lower panels, respectively.

independently dominated by the Pt/C and NiFe catalysts, respectively.

Ohmic loss analysis revealed that greater losses occur at the cathode, mainly due to higher sheet resistance. Importantly, our modeling indicates that this resistance increase does not originate from the electrode itself, but rather from the diaphragm (η_{ohm}^{s}) (Fig. S30, SI). This finding reinforces the role of hydrogen nanobubble trapping within the diaphragm's skin layer as a major contributor to the increased resistance. The small size and strong surface adhesion of hydrogen bubbles lead to longer retention times and higher local resistance near the cathode.[15,16] Additionally, the introduction of catalysts further exacerbated sheet resistance increases at both electrodes (Fig. 3d and Fig. S30, SI), likely due to changes in the porous structure of the catalyst layers that enhance gas bubble entrapment. Given hydrogen's physical characteristics, these effects are more pronounced at the cathode side, amplifying ohmic losses.

Mass transport losses, although minor compared to kinetic and ohmic losses up to 2 A cm^{-2}, were also affected by bubble behavior. During the OER, the use of bare nickel foam resulted in a slightly higher mass transport resistance, which is likely attributed to the inherently higher molecular weight and lower solubility of oxygen bubbles relative to hydrogen bubbles (Fig. 3c).[14,34] However, after catalyst introduction, mass transport resistance notably increased at the cathode, while slightly decreasing at the anode (Fig. 3d). This asymmetry can be explained by the formation of a porous catalyst layer at the cathode, which facilitated the trapping of hydrogen nanobubbles within the micro-gaps near the electrode–diaphragm interface. In conclusion, these findings highlight that optimizing catalyst layers in zero-gap alkaline water electrolyzers requires a dual focus: not only enhancing porosity for gas diffusion but also carefully managing interfacial phenomena—particularly gas bubble-induced increases in ohmic and mass transport resistance at the electrode–diaphragm interface.

8686 | *Energy Environ. Sci.*, 2025, **18**, 8679–8696

This journal is © The Royal Society of Chemistry 2025

Nickel foam cathode behavior: activation and deactivation

Prolonged operation led to distinct surface changes at both electrodes, by electrochemical reactions and electrolyte interactions. After a 24-hour voltage held at 2.0 V, polarization curves (Fig. 4a and Fig. S31, S32, SI) showed increased electrode potential, enhancing overall performance. Over 150 hours, cathode activity initially improved before slightly declining, while the anode showed early degradation followed by partial recovery—indicating dynamic surface restructuring. Ni K-edge X-ray absorption near-edge structure (XANES) analysis revealed shifts in the white-line peak (1s → 4p) to higher energies with increased intensity (Fig. 4b). These findings suggest a decrease in electron density in the Ni d-orbital and an increase in vacant states in the

p-orbital, corresponding to surface Ni atoms bonding with OH$^-$ or H$^+$ ligands and transitioning into an oxidized state during the first 24 hours. Ni K-edge Fourier transformed extended X-ray absorption fine structure (FT-EXAFS) analysis showed a slight increase in the radial distance of the Ni–Ni peak, with no significant loss in intensity (Fig. 4c), suggesting that the bulk metallic structure of nickel foam was preserved with surface modifications occurred. These results are consistent with the formation of α-NiO$_x$ or Ni(OH)$_2$ phases on the surface (Fig. S33, SI), which may contribute to enhanced HER activity by altering Ni's d-band center and its local structure during the initial voltage hold period.[35]

After 150 hours, XANES analysis showed decreases in white-line peak energies, accompanied by reduced intensity, indicating
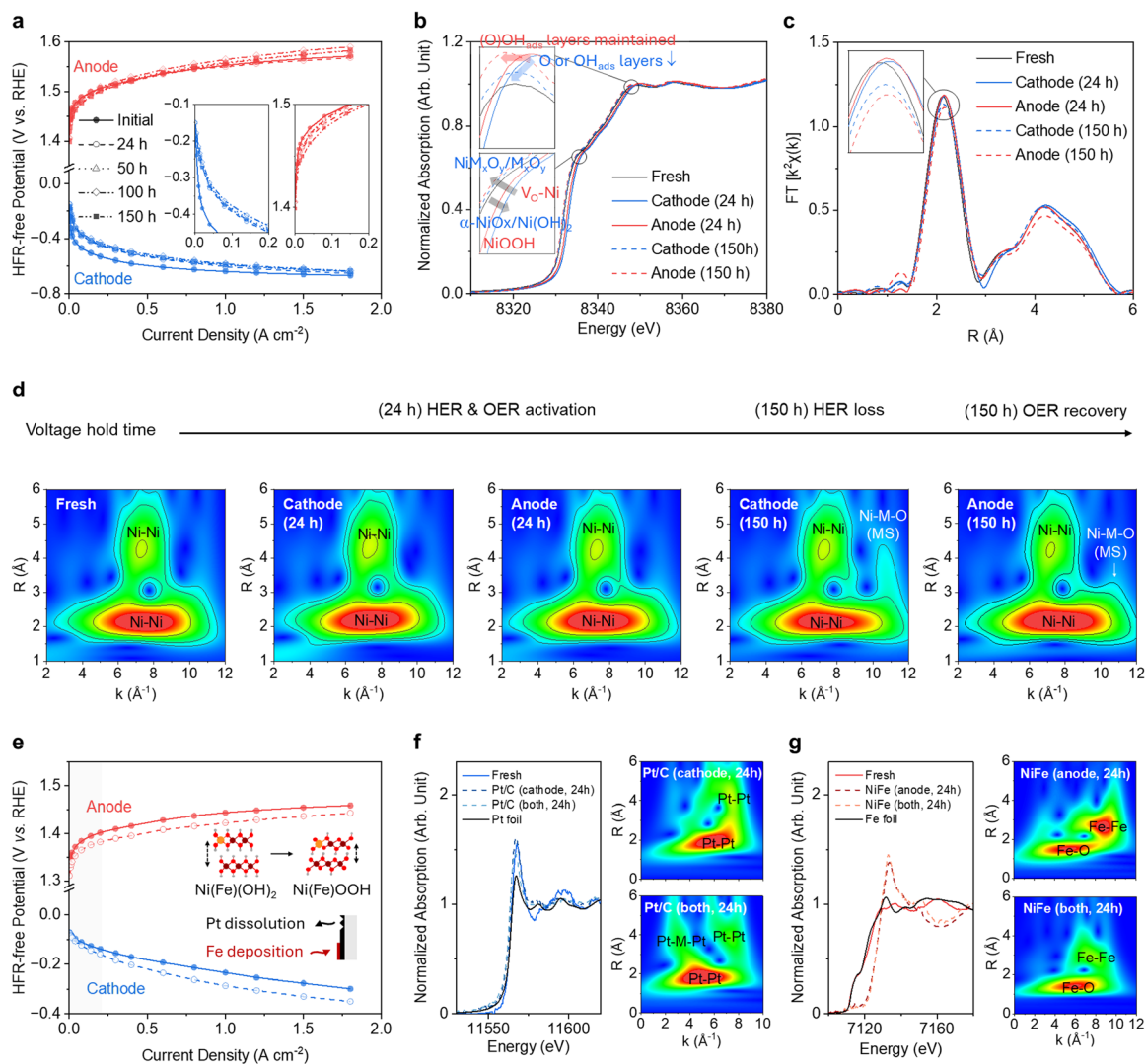

Fig. 4 Study on the activity–structure/property relationship at the cathode and anode under applied cell voltage. (a)–(d) Evolution of potential and properties under a constant 2.0 V voltage hold for up to 150 h without integrated catalysts. HFR-free polarization curves (a). Note that compared to the 100 h measurement, the 150 h results show a slight decrease in HER activity (deactivation) and a slight increase in OER activity (recovery), leading to a modest improvement in the full-cell polarization curve (Fig. S31, SI). Ni K-edge normalized XANES (b), FT-EXAFS (c), and WT-EXAFS (d). Insets in (a)–(c) provide magnified views of each plot. (e)–(g) Potential and property changes before and after a 24 h 2.0 V hold in the Pt/C + NiFe (both) case. HFR-free polarization curves (e). The schematic in (e) illustrates the anticipated changes in the Pt/C cathode catalyst layer and the NiFe anode catalyst layer after voltage application. Pt L-edge normalized XANES ((f), left) and WT-EXAFS ((f), right) for the cathode. Fe K-edge normalized XANES ((g), left) and WT-EXAFS ((g), right) for the anode.

This journal is © The Royal Society of Chemistry 2025

Energy Environ. Sci., 2025, **18**, 8679–8696 | **8687**

increased electron density in the d- and p-orbitals. FT-EXAFS analysis showed reduced Ni–Ni radial distances and intensities, suggesting surface restructuring under reducing conditions. Wavelet transform (WT) analysis identified a multi-scattering Ni–M signal ($\sim$3.5 Å), aligned with the characteristic multi-scattering region observed in the WT analysis of nickel foam when NiFe alloy catalysts were applied under a 24-hour voltage hold (Fig. 4d and Fig. S34, SI). The Ni–M signal indicating metal impurities (Fe, Al, Zn, Mn, Cu, Cr) from the KOH electrolyte and substrate that were incorporated into the nickel foam, shifting electron density and structural order.[36] This impurity-driven modification was further supported by cyclic voltammetry shifts after 24 hours at 2.0 V, mirroring trends seen with intentional Fe(II) introduction (Fig. S33, SI). While moderate Ni–M bonding optimized hydrogen adsorption, excessive accumulation disrupted HER by altering Ni electron density and forming inactive oxide layers, such as NiM_xO_y, or M_xO_y, reducing active surface area and ultimately HER activity.[37]

Nickel foam anode behavior: activation and recovery

XANES analysis during the first 24 hours revealed an increase in Ni oxidation state, evidenced by white-line peak shifts (Fig. 4b), indicating ligand bonding with OH^- or OOH^- species and the formation of $Ni(OH)_2$/NiOOH layers. After 150 hours, a decrease in white-line peak energies suggested a more reduced Ni state. Despite the continued presence of electron-withdrawing OH^-/OOH^- groups (as indicated by sustained peak intensity), this reduction points to the formation of oxygen vacancies, which likely enhance charge redistribution, increase Ni 3d orbital electron density, and stabilize the reduced oxidation state.[38]

FT-EXAFS analysis showed slight increases in Ni–Ni bond distances and intensities, indicating greater structural disorder (Fig. 4c). WT analysis revealed a weak but enhanced multi-scattering signal at $\sim$3.5 Å (Ni–M bonds), suggesting metal impurity incorporation into the NiOOH structure,[36] likely facilitated by oxygen vacancies, which provide sites for metal impurity insertion, although the involvement of other mechanisms cannot be ruled out.[39] Less pronounced Ni–M multi-scattering signals at the cathode indicate that metal ions are more easily adsorbed and reduced on the Ni surface under reducing conditions, forming metallic bonds with Ni. In contrast, under oxidizing conditions, metal ions predominantly exist in oxide forms, which may hinder their incorporation into the NiOOH structure unless sufficient oxygen vacancies are present.[40] Oxygen vacancies and metal insertion could influence the stabilization of the β,γ-phase of NiOOH, which has been associated with enhanced OER activity.[41] Over extended operation ($>$150 h), the interplay between oxygen vacancy formation, γ-NiOOH structural modification, and metal impurity incorporation may modulate OER activity, potentially contributing to transient recovery.

Behavior of Pt/C coated cathode

Voltage holds with the Pt/C (cathode) and Pt/C + NiFe (both) configurations for 24 hours resulted in a decrease in HER activity by 4.7 mV and 14 mV, respectively, at 0.08 A cm^{-2} at the cathode (Fig. 4e and Fig. S35a, b, e, SI). Pt L-edge XANES analysis indicated a decrease in the oxidation state of Pt, with sustained white-line peak intensity, suggesting stable ligand interactions with H^+ or OH^- species (Fig. 4f, left). While Pt reduction alone does not directly imply HER activity loss, additional structural changes, such as active site depletion due to particle growth via Ostwald ripening and coalescence, likely contributed. These processes led to the formation of thermodynamically stable, and compact (111) facets, along with Pt leaching, ultimately reducing active sites and decreasing HER activity. Furthermore, potential carbon corrosion, ionomer scission, or desulfonation may have also contributed to the observed decline.[42]

A more significant decrease in HER activity when NiFe alloy catalysts were simultaneously applied at the anode suggests the possible migration of dissolved Ni or Fe ions from the anode to the cathode. This hypothesis is supported by WT analysis, which revealed a multi-scattering signal near 4.5 Å corresponding to Pt–M–Pt bonds, indicating potential interactions between Pt and migrated metal species (Fig. 4f, right). The migrated ions either physically blocked Pt active sites or formed bonds with Pt, potentially altering its d-band center. This shift in electronic structure displaced hydrogen adsorption energy from its optimal range, thereby reducing reaction rates.[43] Fe and Ni, with lower electronegativities than Pt, may have influenced the electronic structure of Pt through metallic bonding, as indicated by lower white-line peak energies in Pt L-edge XANES analysis. Furthermore, FT-EXAFS analysis revealed a more significant shift in the Pt–Pt peak position under these conditions (Fig. S36a, SI), suggesting that Pt underwent more pronounced local structural changes, such as a reduction in radial distance, likely due to bond formation with Ni and Fe atoms that may have migrated from the anode.

Behavior of NiFe alloy coated anode

A 24-hour voltage hold with NiFe (anode) and Pt/C + NiFe (both) configurations enhanced OER activity by 20 mV at 0.08 A cm^{-2} at the anode (Fig. 4e and Fig. S35c, d, f, SI). Fe K-edge XANES revealed a decreased pre-edge and increased white-line peak intensity, indicating the transformation of NiFe alloy into a Ni(Fe)OOH structure during this period (Fig. 4g, left). His phase change likely contributes to improved OER kinetics through electronic restructuring and Ni–Fe synergy.[44] Supporting this, FT-EXAFS analysis showed a shift in the Fe–Fe bonding peak from 2.1 Å to 1.7 Å, suggesting the coordination with O-based species such as O, OH, or OOH (Fig. S36b, SI). WT-EXAFS further confirmed these ligand interactions, with a strong single-scattering signal at 1.7 Å (Fig. 4g, right). Simultaneously, the Ni K-edge WT-EXAFS analysis demonstrated that Ni atoms on the metallic nickel foam surface formed coordination bonds with Fe, further confirming the formation of a Ni(Fe)OOH structure (Fig. S34, SI). The Fe coordination influenced the Ni^{3+}/Ni^{4+} oxidation states, potentially stabilizing OOH intermediates and increasing the number of active sites, thereby significantly enhancing OER activity.[45] The superior initial OER activity and its further improvement after 24 hours of voltage

8688 | Energy Environ. Sci., 2025, 18, 8679–8696

This journal is © The Royal Society of Chemistry 2025

hold, compared to using nickel foam alone, strongly suggest that Ni(Fe)OOH outperforms NiOOH in OER.[46] While many recent studies indicate that γ-phase Ni(Fe)OOH exhibits superior OER activity over β-phase Ni(Fe)OOH, further structural characterization is required to confirm the specific phase composition.[47]

Interestingly, the OER activity gain after voltage holds in the Pt/C + NiFe configuration was comparable to that with NiFe at the anode alone, suggesting minimal adverse effects from Pt leaching. While Pt ion adsorption onto the Ni(Fe)OOH surface and formation of OER-inactive PtO_x species may have slightly offset performance, these effects were far less pronounced than those from Ni or Fe leaching.[48] The modest OER enhancement in the Pt/C + NiFe configuration likely derives from increased Ni(Fe)OOH formation,[49] supported by Fe K-edge XANES, FT-EXAFS, and WT-EXAFS analyses showing higher Fe oxidation states and stronger oxygen coordination when catalysts were applied to both electrodes (Fig. 4g and Fig. S36, SI). This observation, identified through the integration of our dual-instrumentation reference cell and *ex situ* spectroscopy, reveals electrode cross-talk and its detrimental effect on HER

performance. These findings demonstrate the broader use of the proposed framework in diagnosing inter-electrode interactions and unraveling structure–property–activity relationships under realistic operating conditions. Moreover, the ability to track catalyst evolution and metal migration in recirculating electrolyte systems offers valuable insight for the rational design of more robust and efficient electrocatalysts.

Understanding the interfacial behaviors in a zero-gap alkaline water electrolysis cell

A micro-gap between the electrode and the diaphragm is likely to contribute to increased ohmic resistance by disrupting uniform electrolyte concentration and the elongating ion migration pathways.[14–16,50] Additionally, the accumulation or entrapment of generated hydrogen and oxygen gases within these gaps can create dead zones, reducing the electrochemically active surface area and obstructing ion transport pathways, thereby exacerbating kinetic and ohmic resistances.[34] In this study, the extension of the Zirfon diaphragm was used solely to form an ion channel for the reference electrode, allowing the assumption of uniform ionic conductivity within
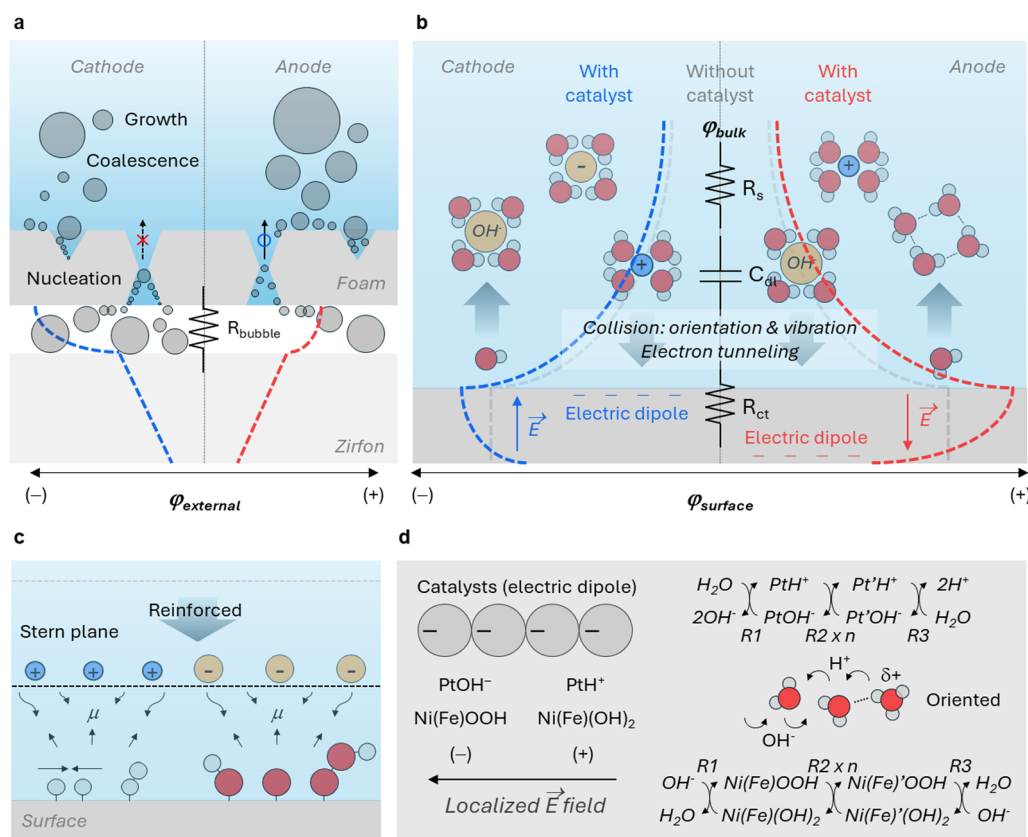

Fig. 5 Schematics of proposed bubble dynamics and localized electric field effects in a zero-gap alkaline water electrolyzer. (a) Bubble evolution stages and local electric potential profiles. Nucleation initiates within pores, particularly in cracks and crevices of the electrode surface, followed by bubble growth as gas diffuses from the dissolved gas boundary layer. If a micro-gap exists between the electrode and diaphragm, trapped bubbles can accumulate, disrupting OH^- ion distribution and increasing ohmic resistance. (b) Electrode–electrolyte interface and electric potential profiles. The localized electric field generated by the catalyst layer facilitates molecular and solvent reorganization in the solution. (c) OHP modification induced by the localized electric field and its impact on intermediates, maintaining a lowered E_a across varying overpotentials. (d) Electric dipole modulation and intermolecular reaction pathways *via* protonation and deprotonation on nanoparticle surfaces under an external electric field. This process follows the Grotthuss mechanism, where charge transfer occurs through a network of hydrogen-bonded water molecules.

the diaphragm. Similarly, the use of nickel foam substrates with identical specifications as the electrode material supports the assumption of uniform ionic conductivity within the electrodes. Under these controlled conditions, although the direct accumulation and trapping of hydrogen bubbles were not observed experimentally, the most plausible factor contributing to the significant difference in ohmic resistance is the ohmic drop caused by micro-gaps.

Fig. 5a illustrates possible bubble behaviors and potential electric profiles at the cathode and anode, constructed based on experimental and modeling results. The higher ohmic resistance observed at the cathode suggests that hydrogen bubbles accumulate in micro-gaps more prominently than oxygen bubbles, leading to a sharp imbalance in OH^- ion concentration and a significant increase in ohmic overpotential. While the electronic resistance within the Ni-based electrode is negligible due to its high conductivity, the measured HFR primarily reflects ionic resistance across the membrane and within the porous electrode. In particular, the ionic conductivity within the electrode can be significantly influenced by the presence of gas bubbles, which reduces the effective electrolyte volume and increases tortuosity. These transport limitations may explain the higher HFR observed at the cathode. This hypothesis aligns with previous findings on gas-induced transport limitations in incomplete zero-gap alkaline electrolysis, where hydrogen's smaller bubble size and greater surface adhesion (pinning effect) compared to oxygen result in longer residence times at the electrode surface.[15–18] The porous structure of nickel foam exacerbates this effect by trapping small gas pockets, transiently increasing resistance by elongating ion migration paths.[51] Additionally, rapid nucleation and dense hydrogen bubble coverage increase the void fraction within micro-gaps, reducing local ionic conductivity.[14] The weaker detachment forces of hydrogen bubbles, due to their lower density and higher surface tension, further facilitate coalescence and the formation of persistent voids that inhibit mass transport.[34] Despite expectations that catalyst introduction would mitigate ohmic resistance, no substantial differences were observed between the electrodes, indicating that the catalyst layer does not effectively suppress nanobubble formation within micro-gaps or enhance mass transfer dynamics. Instead, this suggests that ohmic drop is more significantly influenced by the formation-detachment behavior occurring on the diaphragm surface or within its internal skin layer rather than by the electrode itself. The observed decrease in cathodic ohmic resistance after 150 hours of continuous voltage hold (Fig. S37, SI) may be attributed to the progressive enhancement in hydrogen bubble detachment, which likely altered the interfacial structure to facilitate improved ion transport. This enhancement may stem from a combination of factors, including electrode surface activation, enhanced wetting of the nickel foam or diaphragm, and improved electrolyte penetration within micro-gaps.[52] The fact that this trend similarly appears even after catalyst introduction suggests that the inherently unfavorable characteristics of hydrogen bubbles lead to a more pronounced ohmic drop within micro-gaps, while the interfacial structure gradually improves over time (Fig. S38, SI). Therefore, alternative strategies, such as optimizing substrate porosity, refining the electrode–diaphragm interface architecture, or introducing hydrophilic/hydrophobic surface modifications, may be essential to effectively minimize bubble accumulation and further mitigate ohmic resistance.
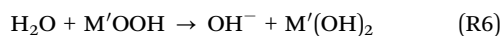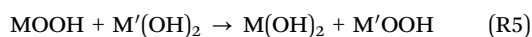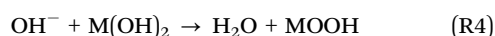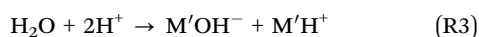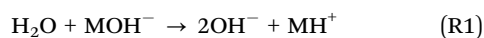
Fig. 5b presents a schematic illustrating how the localized electric field formed within the catalyst layer influences molecular and solvent behavior in solution, along with the resulting surface electric potential distribution. In highly conductive nanoparticles, electron redistribution occurs under an external electric field to shield the field, potentially leading to local charge separation and the induction of nanoscale dipole moments, reinforcing reorganization energy (λ) within the Debye length.[53] This local electric field formation, specifically the polarized electron distribution on the electrode surface,[54] enhances both attractive and repulsive interactions mediated by hydrogen bonding and van der Waals forces.[55] As a result, more adsorbates, solvated ions, and water molecules align systematically at the interface, forming structured layers that influence charge distribution and interfacial stability. Simultaneously, reactant and product diffusion are facilitated through enhanced transport pathways, improving mass transfer efficiency. This phenomenon is well described by models such as the Helmholtz, Stern, and Gouy–Chapman models,[56] which collectively represent the potential gradient extending from the electrode surface to the bulk electrolyte region, where the increased density of balancing balance charges results in a steeper potential gradient. In particular, the formation of a denser and more compact outer Helmholtz plane (OHP) strengthens electrostatic interactions through ion effects, stabilizes reaction intermediates, and mitigates local pH fluctuations *via* a buffering effect.[57–59] These factors collectively contribute to maintaining a thermodynamically lowered energy barrier throughout the reaction process across varying overpotentials, as schematically illustrated in Fig. 5c.

The exponentially increasing A–η relationship and the emergence of an inverted region in the E_a–η relationship observed in our catalyst-integrated Arrhenius-type analysis can be well explained based on Marcus theory.[25] This theory describes intermolecular electron transfer, emphasizing the role of reorganization energy in determining reaction rates. It also predicts the existence of an inverted region beyond a certain overpotential, where excessive spontaneity in free energy leads to an increase in activation energy.[60] In this context, the enhanced interfacial molecular dynamics induced by the localized electric field become the dominant factor in governing reaction kinetics once the energy barrier is sufficiently lowered. The appearance of an inverted E_a region beyond a certain overpotential further supports that, in high-concentration alkaline electrolyte environments, the catalyst-mediated reaction follows the principles of Marcus theory, where intermolecular electron transfer is largely influenced by reorganization processes within the solution. Additionally, terminal oxo and hydroxyl groups formed on the catalyst surface can interact with the hydrogen bonds of surrounding water molecules, modulating local hydrogen bonding networks and influencing OH^- ion transfer.[61] This transfer, occurring *via* the Grotthuss

8690 | *Energy Environ. Sci.*, 2025, **18**, 8679–8696

This journal is © The Royal Society of Chemistry 2025

mechanism,[62] relies on a series of protonation and deprotonation steps and is likely facilitated by a well-oriented water-catalyst arrangement, which is strongly driven by the localized electric field.

Fig. 5d is a schematic illustrating how electric dipoles form on the surfaces of the Pt/C cathode catalyst and NiFe anode catalyst, leading to polarization, and how the proposed surficial molecular reaction mechanism operates for both HER and OER. Within the Pt/C catalyst layer, Pt–OH species dominate in negatively charged regions, while Pt–H species prevail in positively charged regions. Similarly, in the NiFe catalyst layer, negatively charged regions facilitate the formation of $Ni(Fe)(OH)_2$ (Ni^{2+}), while positively charged regions promote the formation of $NiFeOOH$ (Ni^{3+}). Building on these assumptions, we propose a surficial molecular reaction mechanism for both HER and OER, where M represents active catalytic sites, and M' denotes surface sites undergoing protonation or deprotonation during reaction steps:

$$H_2O + MOH^- \rightarrow 2OH^- + MH^+ \tag{R1}$$

$$MH^+ + M'OH^- \rightarrow MOH^- + M'H^+ \tag{R2}$$

$$H_2O + 2H^+ \rightarrow M'OH^- + M'H^+ \tag{R3}$$

$$OH^- + M(OH)_2 \rightarrow H_2O + MOOH \tag{R4}$$

$$MOOH + M'(OH)_2 \rightarrow M(OH)_2 + M'OOH \tag{R5}$$

$$H_2O + M'OOH \rightarrow OH^- + M'(OH)_2 \tag{R6}$$

(R1) and (R3) for HER, and (R4) and (R6) for OER represent the steps where water molecules dissociate or associate, and protons are released to form bonds on the catalyst surface. These steps involve molecular bond breaking, requiring energy to overcome the activation barrier. As a result, (R1) and (R3) are considered η-dependent early stages of the reaction mechanism.[63] In contrast, (R2) involves the movement of charge across different acceptor/donor sites on the catalyst surface, which may occur in a series.[64,65] These steps are less influenced by η and are instead determined by the interfacial dynamics.

In this context, the proposed surficial molecular reaction mechanism effectively explains the observed η dependence of E_a and the A, both with and without integrated catalysts. In the absence of a catalyst, E_a inversely correlates with η, as the energy barriers for reactions (R1) and (R3), being the RDS, are lowered through potential changes, thereby enhancing reaction kinetics. Notably, OER benefits from a more efficient reduction in activation energy than HER, indicating that (R1) and (R3) are more effectively promoted during OER. This results in superior reaction pathways and improved kinetics for OER under similar conditions. Conversely, the inefficiency of reaction (R2), due to the limited surficial properties of nickel foam for charge transfer leads to a decreased A. In the presence of a catalyst, the E_a becomes independent of the η due to inherently lowered energy barriers and a reinforced OHP effect, allowing reactions (R1) and (R3) to proceed rapidly across varying overpotentials. Instead, the A increases exponentially with η, as (R2), being the RDS, and benefits from the rapid responsiveness of interfacial dynamics to overpotential changes, thereby accelerating

reaction kinetics. This intermolecular charge transfer can be further enhanced by the more structured alignment of surrounding water molecules. Overall, the proposed surficial molecular reaction mechanism logically explains the observed relationships among activation energy, the pre-exponential factor, and overpotential, supporting the hypothesis that localized electric fields within the catalyst layer enhance intermolecular dynamics at the interface, thereby improving reaction efficiency. While the underlying governing mechanisms are similar for Pt/C at the cathode and NiFe at the anode, the extent and magnitude of surface reorganization and reaction efficiency improvements will vary. Specifically, the earlier inversion behavior at higher overpotentials and the more rapid exponential increase of A observed in NiFe suggest that the localized electric field effect is more pronounced at the NiFe anode. The schematic presented in Fig. 5 is a qualitative hypothesis derived from electrochemical observations using the dual-instrumentation tool. While it aims to visualize potential interfacial behavior during AWE operation, further validation through theoretical approaches such as density functional theory, molecular dynamics, or computational fluid dynamics will be necessary to confirm and refine the proposed mechanisms.

Conclusion

This study presents a separator-extension reference electrode strategy coupled with a dual-instrumentation setup, enabling real-time, independent monitoring of HER and OER kinetics in zero-gap alkaline water electrolysis. By integrating a commercial Hg/HgO reference electrode, we successfully decouple the behaviors of the electrodes, providing high-resolution diagnostics of individual half-reactions under operational conditions. Our results challenge the conventional assumption that HER is inherently faster than OER in alkaline media. Instead, we reveal that HER is more kinetically hindered, especially in catalyst-free systems, due to higher charge transfer resistance and mass transport limitations. Through Arrhenius-type analysis, we uncover a transition in kinetic regimes: from Butler–Volmer behavior in the absence of catalysts to Marcus-type behavior when particle-based catalysts are present. This shift is driven by localized electric fields that promote structured water alignment and interfacial reorganization, ultimately enhancing bimolecular charge transfer. The proposed surficial molecular mechanism not only explains this kinetic shift but also provides a framework for catalyst and electrode architecture design aimed at improving interfacial charge dynamics. Combined with *operando* XAFS analyses, we also track catalyst transformation, metal migration, and the formation of active phases, offering insights into degradation and activation processes under realistic electrolysis conditions.

Looking forward, this study offers a powerful tool for benchmarking catalyst performance, understanding degradation mechanisms, and guiding materials discovery. Future work will focus on adapting this strategy for long-term durability studies. These insights will support the development of next-generation alkaline electrolysis systems.

This journal is © The Royal Society of Chemistry 2025

Energy Environ. Sci., 2025, **18**, 8679–8696 | **8691**

Methods

Materials

Nickel foam ($\sim$300 µm, RECEMAT BV) and nickel mesh ($\sim$300 µm, Dorstener Drahtwerke) were used as electrode substrates, while Zirfon™ Perl UTP ($\sim$220 µm and $\sim$500 µm, Agfa) was used as the diaphragm. Pt/HSC (47.5%, TEC10E50E, Tanaka Kikinzoku Kogyo), NiFe (Fe : Ni = 0.55 : 0.45, 97% metal basis metals basis, Sigma-Aldrich), NiO (99.8% metal basis, Sigma-Aldrich), and Co_3O_4 (99% metal basis, US Research Nanomaterials) were employed as catalysts, with Nafion™ (D2020, Chemours) serving as the ionomer binder. KOH ($>$85% KOH basis, EMSURE) was used for 30 wt% (1.27 g mL^{-1}) electrolyte preparation.

Ink preparation

The Ni-based substrates were soaked in a 1 M HNO$_3$ mild acidic solution for at 10 minutes before cell assembly or catalyst loading, followed by thorough washing with DI water. The catalyst ink was prepared by mixing catalysts with D2020 Nafion in a 1 : 3 (w : w) ratio of deionized (DI) water to 1-propanol (nPA), followed by sonication in an ice bath for over 30 minutes and subsequent aging (stirring at room temperature) for approximately one day. The ink was then applied onto nickel foam via hand-spraying. For the ink composition, Pt/C was prepared with a solid content of 4% and an ionomer-to-catalyst ratio of 0.5, while NiFe, NiO, and Co_3O_4 inks had a solid content of 2% and an ionomer-to-metal ratio of 0.3. The loading amounts were controlled as follows: Pt/C was applied at 0.5 and 1.0 mg cm^{-2}, NiFe at 0.5, 1.0, and 2.0 mg cm^{-2}, and NiO and Co_3O_4 at 2.0 mg cm^{-2}. After spray coating, the electrodes were dried at 60 °C for at least 15 minutes, followed by additional drying at room temperature for over 24 hours to ensure proper adhesion and solvent evaporation.

Hardware for reference electrode integrated AWE cell setup

An alkaline single cell, as published by Forschungszentrum Jülich (FZJ), was used in this study.[66] This setup included backplates, Ni flow fields, PTFE sealing gaskets, centering pins, and Ni current collectors. The electrode gasket was designed with a 5 × 5 cm^2 window size and a 0.2 mm thickness. The cell hardware featured endplates designed for compression by 25%, secured using eight bolts that were tightened crosswise in sequential steps of 3, 5, and 10 Nm. The nickel foam, nickel mesh, catalyst coated nickel foam and Zirfon™ Perl UTP diaphragm (pre-soaked for over 1 hour to ensure full wetting) were sealed and compressed by PTFE gaskets. The diaphragm gasket featured a 4 × 4 cm^2 window size and was designed as an open-type structure with a 2 mm gap to accommodate the sealing of the extension strip. Depending on the thickness of the diaphragm used, the diaphragm gasket was configured with either 0.2 mm or 0.4 mm thickness. A PTFE-based bath was custom-made to house both the extension strip and the reference electrode. The housing rod height and spacing were designed with careful consideration to minimize drying of the extension strip while preventing short within the system and insulating against heat generated from the cell. Additionally, an insulator patch was incorporated to further mitigate thermal effects, ensuring stable operation of the reference electrode setup. A customized Hg/HgO reference electrode (30% KOH filling solution, Koslow) was used, with a +0.86 V calibration for RHE conversion, determined using a RDE technique in an H$_2$-saturated 30 wt% KOH solution.

Cell testing conditions and procedures

All cell tests were conducted using built-in-house test stations, which included two KOH tanks with a balancing line, pumps, temperature control, an electrical power supply, and a cell potential measurement system. All cells operated under electrolyte circulation conditions, with a cathode/anode flow rate of 50 mL min^{-1} at 80 °C and ambient pressure.[67] The electrolyte temperature was precisely controlled using a thermocouple at each inlet, while heater pads on the hardware end plates regulated the cell temperature, with a thermocouple inserted into the anode flow field ensuring accurate monitoring. Following the standard cell evaluation configuration, the potentiostat's working and sensing leads were connected to the cathode, while the counter, sensing lead, and reference lead were connected to the anode. For the auxiliary electrometer, Ch1's (+) lead was connected to the cathode and (−) lead to the anode, whereas Ch2's (+) lead was connected to the anode and (−) lead to the cathode. Using the synchronized hubs provided by Gamry Instruments, full-cell polarization and impedance measurements were conducted while simultaneously measuring the potential and impedance of both electrodes.

After an initial cell heat-up and equilibration period of over 30 minutes, a pre-conditioning step at 2.0 V for 10 minutes was conducted before performance testing. Subsequently, a galvanostatic step-wise polarization curve was recorded, starting from 1.8 A cm^{-2} down to 0.004 A cm^{-2} in the cathodic direction, followed by a sweep back from 0.004 A cm^{-2} to 1.8 A cm^{-2} in the anodic direction, with a 1-minute holding time at each step. For polarization curve evaluation, the average of the last 40 data points at the end of each holding time was used for comparison. Next, a durability test at a constant cell voltage of 2.0 V for 24 hours was conducted. After this constant voltage hold, another polarization curve measurement was recorded following the same methodology. For the 150-hour long-term durability test, polarization curves were recorded at 24 h, 50 h, 100 h, and 150 h, with a 2 V voltage hold preceding each measurement. All polarization curve measurements were accompanied by galvanostatic step-wise impedance measurements ranging from 1 Hz to 10 kHz, with the real impedance value (Z) at frequencies above 1 kHz used for HFR correction. While many previous studies use x-intercept via interpolation for HFR correction, this study instead utilized clear real Z values above 1 kHz to account for ohmic resistance within the electrode layer and exclude noise at high frequency introduced by the reference electrode cell setup. The same selected frequency range was applied to the cathode, anode, and full cell measurements for consistency. The AC amplitude for impedance measurements was set to 5% of the DC current. All performance and impedance data presented in this study were

recorded using a Gamry potentiostat/galvanostat/ZRA with a 20A booster and an auxiliary electrometer (Reference 3000AE). EIS and DRT analysis were performed using a Gamry Echem Analyst software.

Arrhenius-type analysis and equation derivation

Polarization curve and impedance measurements at 40 °C, 60 °C, and 80 °C were conducted after a temperature equilibrium period of at least 2 hours. Using temperature-dependent modeling (ANL), the equilibrium potentials for HER and OER, as well as the equilibrium voltage for overall water electrolysis, were calculated and utilized to construct Arrhenius plots. Subsequently, cubic spline fitting and interpolation were applied to generate E_a vs. η and A vs. η plots. To further analyze these relationships, eqn (2) was derived by integrating the Arrhenius-type model equation with a simplified Butler–Volmer model equation. Exponential fitting was then performed using semi-empirical eqn (3) ($y = B \exp(A \times x)$), which was implemented in Origin software (C-type function).

Modeling study

To calculate the change in equilibrium potential (E_N) due to temperature, both the entropy and the pH terms were considered. Given that $\Delta G = -T\Delta S$ (the temperature dependence of the equilibrium potential is dominated by the entropy term and thus ΔH is assumed to be 0), and using the equation $\Delta G = -nFE$, the potential correction due to entropy can be calculated as follows:

$$E_S(T) = \frac{ST}{nF}$$

$$E_0(T) = E_0 + E_S(T)$$

$$E_N(T) = E_0(T) + \frac{RT}{nF}\log\left(\frac{(p^c - p_{sv})(p^a - p_{sv})^{0.5}}{p_0^{3/2}a_{H_2O}}\right)$$

where S is the entropy, T is the temperature, n is electron transfer number, F is the Faraday constant, p^a and p^c are the anode and cathode pressures, respectively, p_{sv} is the saturation vapor pressure (here we assume that the partial pressure of hydrogen at the cathode is the total pressure at the cathode less the saturation vapor pressure, and similarly for the oxygen partial pressure at the anode), and a_{H_2O} is the activity of water. The voltage breakdown model partitions the overall cell voltage into contributions from thermodynamic, kinetic (activation), ohmic, and mass transfer losses, for each half-cell. The Nernst

potential for each half cell is corrected for temperature, pressure, and pH changes (activity) (eqn (4)). Special consideration is given to the activity of [OH⁻] due to its high concentration.

Activation overpotential is reproduced using a modified Butler–Volmer expression that relies on a hyperbolic sine function, a Tafel slope, an exchange current density, and bubble coverage term to account for the reduction in active area due to bubble adherence to the electrode and catalyst surface (eqn (6)). The Tafel slope and exchange current density are derived from experimental data, while the bubble coverage term is a function of current density, pressure, and temperature. In addition, a mass transfer overpotential is included, derived from experimental polarization curves, and defined as any non-linearity in the polarization behavior, evident primarily at higher current densities (eqn (7)).

The overall ohmic losses are broken down into two parts—electrode and diaphragm contributions. The electrode overpotential is estimated using a distributed current approach, which relies on the sheet resistance of the nickel foams and catalyst layers, and the Tafel slope determined from the kinetic modeling. The catalyst layer thickness, estimated to be around 2–3 μm based on catalyst density, porosity, and mass. For the diaphragm, the ohmic overpotential is computed based on the sheet resistance, electrolyte conductivity, porosity, and tortuosity of the Zirfon diaphragm and cross-checked against published data (eqn (5)). The resulting diaphragm resistance is around 153 mΩ cm². Experimental impedance data guided the allocation of diaphragm resistance between the half-cells, with the cathodic side receiving 60–75% due to nanobubble effects and local concentration shifts, and the remaining resistance attributed to the anodic side.

The transmission line model (TLM) analyzes EIS data by fitting it to an equivalent circuit representing the impedance behavior of both half-cells and the full cell. This circuit consists of resistive, inductive, and capacitive elements. Specifically, the resistances include ohmic resistance, ion transfer resistance, charge transfer resistance, and mass transfer resistance. The ohmic resistance accounts for the bulk resistance of the electrolyte, electrodes, membrane, and other system components. The ion transfer resistance reflects the resistance associated with OH⁻ ion transport. The charge transfer resistance corresponds to the resistance encountered during HER and OER processes. The mass transfer resistance represents the limitations related to gas transport between the electrode and electrolyte. These resistance values were extracted through TLM fitting using the ZView software.
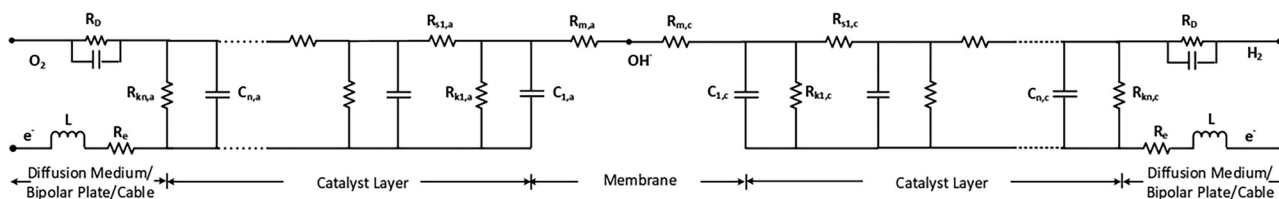
The voltage breakdown model was calibrated against experimental polarization data and electrochemical impedance spectroscopy (EIS) measurements obtained at 1 atm and 80 °C. In these experiments, the individual overpotentials of the anode and cathode were determined and the overall diaphragm resistance was divided based on observed trends.

XAS measurements

X-ray absorption spectroscopy (XAS) measurements were performed at the Pt L_3-edge, Ni K-edge, and Fe K-edge in fluorescence mode for all electrodes. Both X-ray absorption near-edge structure (XANES) and extended X-ray absorption fine structure (EXAFS) analyses were conducted at the 6D UNIST-PAL beamline of the Pohang Accelerator Laboratory (PAL), Republic of Korea (PLS-II), operating at an electron energy of 2.5 GeV and a top-up stored current of 300 mA. Monochromatic X-rays generated from a bending magnet were selected using a Si(111) double-crystal monochromator, with beam intensities reduced by 10–30%, depending on the target element, to suppress higher-order harmonics. The collected spectra were processed using Larch software, including background subtraction and normalization. Additionally, wavelet transform (WT) analysis of the EXAFS spectra was performed to distinguish the specific contribution of each element to the overall EXAFS signal.

Author contributions

W. Y. N. and M. S. conceived the research idea and designed the experiments. W. Y. N. conducted the majority of electrochemical measurements and performed data analysis. M. S. supervised and managed the overall research project. S. J. K. and J. P. conducted cell modeling. W. Y. N., S. L., and T. J. S. performed the X-ray absorption spectroscopy experiments and data analysis. W. Y. N., M. S., S. J. K., S. L., J. P., and T. J. S. jointly contributed to manuscript preparation. All authors reviewed and edited the final manuscript.

Conflicts of interest

The authors declare no competing interests.

Data availability

All data supporting the findings of this study are available within the article and its SI. The supplementary information file contains additional experimental details, discussions, extended datasets, figures (Fig. S1–S38), comprehensive numerical data (S1–S4), and supporting literature related to the study's findings. See DOI: **https://doi.org/10.1039/d5ee03044g**

Additional data or materials used in this study are available from the corresponding author upon reasonable request.

Acknowledgements

References

1 O. Schmidt, A. Gambhir, I. Staffell, A. Hawkes, J. Nelson and S. Few, Future cost and performance of water electrolysis: An expert elicitation study, *Int. J. Hydrogen Energy*, 2017, **42**(52), 30470–30492.

2 G. Glenk and S. Reichelstein, Economics of converting renewable power to hydrogen, *Nat. Energy*, 2019, **4**(3), 216–222.

3 A. Buttler and H. Spliethoff, Current status of water electrolysis for energy storage, grid balancing and sector coupling *via* power-to-gas and power-to-liquids: A review, *Renewable Sustainable Energy Rev.*, 2018, **82**, 2440–2454.

4 C. Hu, L. Zhang and J. Gong, Recent progress made in the mechanism comprehension and design of electrocatalysts for alkaline water splitting, *Energy Environ. Sci.*, 2019, **12**(9), 2620–2645.

5 A. Hartig-Weiß, M. Bernt, A. Siebel and H. A. Gasteiger, A platinum micro-reference electrode for impedance measurements in a PEM water electrolysis cell, *J. Electrochem. Soc.*, 2021, **168**(11), 114511.

6 Z. Siroma, R. Kakitsubo, N. Fujiwara, T. Ioroi, S.-I. Yamazaki and K. Yasuda, Compact dynamic hydrogen electrode unit as a reference electrode for PEMFCs, *J. Power Sources*, 2006, **156**(2), 284–287.

7 A.-T. Tran, F. Huet, K. Ngo and P. Rousseau, Artefacts in electrochemical impedance measurement in electrolytic solutions due to the reference electrode, *Electrochim. Acta*, 2011, **56**(23), 8034–8039.

8 R. Zeng, R. C. Slade and J. R. Varcoe, An experimental study on the placement of reference electrodes in alkaline polymer electrolyte membrane fuel cells, *Electrochim. Acta*, 2010, **56**(1), 607–619.

9 P. Leuaa, M. R. Kraglund and C. Chatzichristodoulou, Decoupling of reaction overpotentials and ionic transport losses within 3D porous electrodes in zero-gap alkaline electrolysis cells, *Electrochim. Acta*, 2023, **470**, 143306.

10 E. J. Dickinson and A. J. Wain, The Butler-Volmer equation in electrochemical theory: Origins, value, and practical application, *J. Electroanal. Chem.*, 2020, **872**, 114145.

11 R. C. Kurchin, D. Gandhi and V. Viswanathan, Nonequilibrium Electrochemical Phase Maps: Beyond Butler–Volmer Kinetics, *J. Phys. Chem. Lett.*, 2023, **14**(35), 7802–7807.

12 A. Y. Faid, L. Xie, A. O. Barnett, F. Seland, D. Kirk and S. Sunde, Effect of anion exchange ionomer content on electrode performance in AEM water electrolysis, *Int. J. Hydrogen Energy*, 2020, **45**(53), 28272–28284.

13 M. Ranz, B. Grabner, B. Schweighofer, H. Wegleiter and A. Trattner, Dynamics of anion exchange membrane electrolysis: Unravelling loss mechanisms with electrochemical impedance spectroscopy, reference electrodes and distribution of relaxation times, *J. Power Sources*, 2024, **605**, 234455.

14 R. L. G. Barros, M. H. Kelleners, L. van Bemmel, T. V. van der Leegte, J. van der Schaaf and M. T. de Groot, Elucidating the increased ohmic resistances in zero-gap alkaline water electrolysis, *Electrochim. Acta*, 2024, **507**, 145161.

15 J. Bleeker, C. van Kasteren, J. R. van Ommen and D. A. Vermaas, Gas bubble removal from a zero-gap alkaline electrolyser with a pressure swing and why foam electrodes might not be suitable at high current densities, *Int. J. Hydrogen Energy*, 2024, **57**, 1398–1407.

16 J. Lee, A. Alam, C. Park, S. Yoon and H. Ju, Modeling of gas evolution processes in porous electrodes of zero-gap alkaline water electrolysis cells, *Fuel*, 2022, **315**, 123273.

17 S. Nag, Y. Tomo, H. Teshima, K. Takahashi and M. Kohno, Dynamic interplay between interfacial nanobubbles: oversaturation promotes anisotropic depinning and bubble coalescence, *Phys. Chem. Chem. Phys.*, 2021, **23**(43), 24652–24660.

18 S. Ansari and D. Nobes, The effect of three-phase contact line pinning during the passage of an isolated bubble through a confining pore, *Phys. Fluids*, 2021, **33**(5), 053310.

19 Z. D. He, Y. X. Chen, E. Santos and W. Schmickler, The pre-exponential factor in electrochemistry, *Angew. Chem., Int. Ed.*, 2018, **57**(27), 7948–7956.

20 L. Chen, Q. Xu and S. W. Boettcher, Kinetics and mechanism of heterogeneous voltage-driven water-dissociation catalysis, *Joule*, 2023, **7**(8), 1867–1886.

21 D. T. Limmer, A. P. Willard, P. Madden and D. Chandler, Hydration of metal surfaces can be dynamically heterogeneous and hydrophobic, *Proc. Natl. Acad. Sci. U. S. A.*, 2013, **110**(11), 4200–4205.

22 K. Takahashi, H. Nakano and H. Sato, A polarizable molecular dynamics method for electrode–electrolyte interfacial electron transfer under the constant chemical-potential-difference condition on the electrode electrons, *J. Chem. Phys.*, 2020, **153**(5), 054126.

23 I. T. McCrum and M. T. Koper, The role of adsorbed hydroxide in hydrogen evolution reaction kinetics on modified platinum, *Nat. Energy*, 2020, **5**(11), 891–899.

24 G. Gonella, E. H. Backus, Y. Nagata, D. J. Bonthuis, P. Loche, A. Schlaich, R. R. Netz, A. Kühnle, I. T. McCrum and M. T. Koper, Water at charged interfaces, *Nat. Rev. Chem.*, 2021, **5**(7), 466–485.

25 R. A. Marcus, Electron transfer reactions in chemistry theory and experiment, *J. Electroanal. Chem.*, 1997, **438**(1–2), 251–259.

26 M. Schalenbach, G. Tjarks, M. Carmo, W. Lueke, M. Mueller and D. Stolten, Acidic or alkaline? Towards a new perspective on the efficiency of water electrolysis, *J. Electrochem. Soc.*, 2016, **163**(11), F3197.

27 D. Jang, H.-S. Cho and S. Kang, Numerical modeling and analysis of the effect of pressure on the performance of an alkaline water electrolysis system, *Appl. Energy*, 2021, **287**, 116554.

28 H. S. Harned, The activity coefficient of sodium hydroxide in aqueous solution, *J. Am. Chem. Soc.*, 1925, **47**(3), 676–684.

29 K. Neyerlin, W. Gu, J. Jorne, A. Clark and H. A. Gasteiger, Cathode catalyst utilization for the ORR in a PEMFC: Analytical model and experimental validation, *J. Electrochem. Soc.*, 2007, **154**(2), B279.

30 N.V., A.-G. Technical Data Sheet – Zirfon PERL UTP 500, Separator membrane for alkaline electrolysis. Agfa, 2020. **https://www.agfa.com/specialty-products/wp-content/uploads/sites/8/2020/06/TDS_ZIRFON_PERL_UTP_500_20200525.pdf** (accessed 2025 April 23).

31 J. Rodríguez, S. Palmas, M. Sánchez-Molina, E. Amores, L. Mais and R. Campana, Simple and precise approach for determination of Ohmic contribution of diaphragms in alkaline water electrolysis, *Membranes*, 2019, **9**(10), 129.

32 L.-X. Mao, L.-Y. Li and B. Kim, Modelling of multi-species transport in concrete under the action of external electric field: Influence of the overpotential at electrode–electrolyte interfaces, *J. Electroanal. Chem.*, 2022, **907**, 116079.

33 L. Hourng; T. Tsai and M. Lin, *The analysis of energy efficiency in water electrolysis under high temperature and high pressure*, In *IOP Conference Series: Earth and Environmental Science*, 2017, IOP Publishing, vol. 93, p. 012035.

34 A. Angulo, P. van der Linde, H. Gardeniers, M. Modestino and D. F. Rivas, Influence of bubbles on the energy conversion efficiency of electrochemical reactors, *Joule*, 2020, **4**(3), 555–579.

35 C. Liu, B. Sheng, Q. Zhou, Y. Xia, Y. Zou, P. J. Chimtali, D. Cao, Y. Chu, S. Zhao and R. Long, Manipulating d-band center of nickel by single-iodine-atom strategy for boosted alkaline hydrogen evolution reaction, *J. Am. Chem. Soc.*, 2024, **146**(39), 26844–26854.

36 M. Demnitz, Y. M. Lamas, R. L. G. Barros, A. D. L. den Bouter, J. van der Schaaf and M. T. de Groot, Effect of iron addition to the electrolyte on alkaline water electrolysis performance, *iScience*, 2024, **27**(1), 108695.

37 H. Engell, Stability and breakdown phenomena of passivating films, *Electrochim. Acta*, 1977, **22**(9), 987–993.

38 R. Sarangi, X-ray absorption near-edge spectroscopy in bioinorganic chemistry: Application to M–O2 systems, *Coord. Chem. Rev.*, 2013, **257**(2), 459–472.

39 H. Xiao, H. Shin and W. A. Goddard III, Synergy between Fe and Ni in the optimal performance of (Ni, Fe) OOH catalysts for the oxygen evolution reaction, *Proc. Natl. Acad. Sci. U. S. A.*, 2018, **115**(23), 5872–5877.

40 A. Mavrič, M. Fanetti, Y. Lin, M. Valant and C. Cui, Spectro-electrochemical tracking of nickel hydroxide reveals its irreversible redox states upon operation at high current density, *ACS Catal.*, 2020, **10**(16), 9451–9457.

This journal is © The Royal Society of Chemistry 2025

Energy Environ. Sci., 2025, **18**, 8679–8696 | **8695**

41 W. Chen, J. Shi, Y. Wu, Y. Jiang, Y. C. Huang, W. Zhou, J. Liu, C. L. Dong, Y. Zou and S. Wang, Vacancy-induced catalytic mechanism for alcohol electrooxidation on nickel-based electrocatalyst, *Angew. Chem., Int. Ed.*, 2024, **63**(4), e202316449.

42 N. Goswami, A. N. Mistry, J. B. Grunewald, T. F. Fuller and P. P. Mukherjee, Corrosion-induced microstructural variability affects transport-kinetics interaction in PEM fuel cell catalyst layers, *J. Electrochem. Soc.*, 2020, **167**(8), 084519.

43 E. Skúlason, V. Tripkovic, M. E. Björketun, S. Gudmundsdóttir, G. Karlberg, J. Rossmeisl, T. Bligaard, H. Jónsson and J. K. Nørskov, Modeling the electrochemical hydrogen oxidation and evolution reactions on the basis of density functional theory calculations, *J. Phys. Chem. C*, 2010, **114**(42), 18182–18197.

44 D. Friebel, M. W. Louie, M. Bajdich, K. E. Sanwald, Y. Cai, A. M. Wise, M.-J. Cheng, D. Sokaras, T.-C. Weng and R. Alonso-Mori, Identification of highly active Fe sites in (Ni, Fe)OOH for electrocatalytic water splitting, *J. Am. Chem. Soc.*, 2015, **137**(3), 1305–1313.

45 H. Yang, C. Dong, H. Wang, R. Qi, L. Gong, Y. Lu, C. He, S. Chen, B. You and H. Liu, Constructing nickel–iron oxyhydroxides integrated with iron oxides by microorganism corrosion for oxygen evolution, *Proc. Natl. Acad. Sci. U. S. A.*, 2022, **119**(20), e2202812119.

46 B. Kim, M. K. Kabiraz, J. Lee, C. Choi, H. Baik, Y. Jung, H.-S. Oh, S.-I. Choi and K. Lee, Vertical-crystalline Fe-doped β-Ni oxyhydroxides for highly active and stable oxygen evolution reaction, *Matter*, 2021, **4**(11), 3585–3604.

47 F. Dionigi, Z. Zeng, I. Sinev, T. Merzdorf, S. Deshpande, M. B. Lopez, S. Kunze, I. Zegkinoglou, H. Sarodnik and D. Fan, In-situ structure and catalytic mechanism of NiFe and CoFe layered double hydroxides during oxygen evolution, *Nat. Commun.*, 2020, **11**(1), 2522.

48 X. Lyu, J. Yang and A. Serov, Is Pt dissolution a concern from the counter electrode in electrochemical oxygen evolution reaction?, *Electrochim. Acta*, 2024, **501**, 144824.

49 H. Becker, J. Murawski, D. V. Shinde, I. E. Stephens, G. Hinds and G. Smith, Impact of impurities on water electrolysis: a review, *Sustainable Energy Fuels*, 2023, **7**(7), 1565–1603.

50 X. Deng, F. Yang, Y. Li, J. Dang and M. Ouyang, Quantitative study on gas evolution effects under large current density in zero-gap alkaline water electrolyzers, *J. Power Sources*, 2023, **555**, 232378.

51 D. Lohse and X. Zhang, Surface nanobubbles and nanodroplets, *Rev. Mod. Phys.*, 2015, **87**(3), 981–1035.

52 R. Iwata, L. Zhang, K. L. Wilke, S. Gong, M. He, B. M. Gallant and E. N. Wang, Bubble growth and departure modes on wettable/non-wettable porous foams in alkaline water splitting, *Joule*, 2021, **5**(4), 887–900.

53 S. K. Ghosh and T. Pal, Interparticle coupling effect on the surface plasmon resonance of gold nanoparticles: from theory to applications, *Chem. Rev.*, 2007, **107**(11), 4797–4862.

54 B.-Y. Wen, J.-S. Lin, Y.-J. Zhang, P. M. Radjenovic, X.-G. Zhang, Z.-Q. Tian and J.-F. Li, Probing electric field distributions in the double layer of a single-crystal electrode with angstrom spatial resolution using Raman spectroscopy, *J. Am. Chem. Soc.*, 2020, **142**(27), 11698–11702.

55 H.-J. Butt, Measuring electrostatic, van der Waals, and hydration forces in electrolyte solutions with an atomic force microscope, *Biophys. J.*, 1991, **60**(6), 1438–1444.

56 M. A. Brown, G. V. Bossa and S. May, Emergence of a stern layer from the incorporation of hydration interactions into the Gouy–Chapman model of the electrical double layer, *Langmuir*, 2015, **31**(42), 11477–11483.

57 D. Strmcnik, K. Kodama, D. Van der Vliet, J. Greeley, V. R. Stamenkovic and N. Marković, The role of non-covalent interactions in electrocatalytic fuel-cell reactions on platinum, *Nat. Chem.*, 2009, **1**(6), 466–472.

58 A. Goyal and M. T. Koper, The interrelated effect of cations and electrolyte pH on the hydrogen evolution reaction on gold electrodes in alkaline media, *Angew. Chem., Int. Ed.*, 2021, **60**(24), 13452–13462.

59 A. Goyal, S. Louisia, P. Moerland and M. T. Koper, Cooperative effect of cations and catalyst structure in tuning alkaline hydrogen evolution on Pt electrodes, *J. Am. Chem. Soc.*, 2024, **146**(11), 7305–7312.

60 P. Suppan The Marcus inverted region, *Photoinduced Electron Transfer IV* 2005, pp. 95–130.

61 M. E. Tuckerman, D. Marx and M. Parrinello, The nature and transport mechanism of hydrated hydroxide ions in aqueous solution, *Nature*, 2002, **417**(6892), 925–929.

62 M. Meuwly, A. Bach and S. Leutwyler, Grotthus-Type and Diffusive Proton Transfer in 7-Hydroxyquinoline (NH3) n Clusters, *J. Am. Chem. Soc.*, 2001, **123**(46), 11446–11453.

63 T. Binninger, A. Heinritz and R. Mohamed, Ideal gas reference for association/dissociation reactions: Concentration bias and kinetic reference voltage/potentials in electrolysis, *J. Chem. Phys.*, 2023, **158**(12), 124129.

64 J. O. M. Bockris, Kinetics of activation controlled consecutive electrochemical reactions: anodic evolution of oxygen, *J. Chem. Phys.*, 1956, **24**(4), 817–827.

65 D. Sepa, M. Vojnovic and A. Damjanovic, Reaction intermediates as a controlling factor in the kinetics and mechanism of oxygen reduction at platinum electrodes, *Electrochim. Acta*, 1981, **26**(6), 781–793.

66 C. Karacan, F. P. Lohmann-Richters, G. P. Keeley, F. Scheepers, M. Shviro, M. Müller, M. Carmo and D. Stolten, Challenges and important considerations when benchmarking single-cell alkaline electrolyzers, *Int. J. Hydrogen Energy*, 2022, **47**(7), 4294–4303.

67 M. Shviro, S. Y. Kang, F. D. Campos, V. Larson, S. Maurya and D. P. Leonard, Standardization and best practices in single-cell testing for liquid alkaline water electrolysis, *Front. Energy Res.*, 2025, **13**, 1554086.

8696 | *Energy Environ. Sci.*, 2025, **18**, 8679–8696

This journal is © The Royal Society of Chemistry 2025